Development of battery architecture based on conducting and insulating nanotubes that enhances energy density and thermal stability

エネルギー密度と耐熱性を向上する導電性・絶縁性ナノチューブベース電池アーキテクチャの開発

February 2023

Kentaro KANEKO

金子 健太郎

Development of battery architecture based on conducting and insulating nanotubes that enhances energy density and thermal stability

エネルギー密度と耐熱性を向上する導電性・絶縁性ナノチューブベース電池アーキテクチャの開発

February 2023

Waseda University
Graduate School of Advanced Science and Engineering
Department of Applied Chemistry
Research on Chemical Engineering

Kentaro KANEKO

金子 健太郎

Content

Thesis organization

This thesis consists of five chapters that describe the research regarding the development of battery architecture based on conducting carbon nanotube (CNT) and insulating boron nitride nanotube (BNNT) and improvement of battery performance on thermal stability and energy density.

Chapter 1 is the introduction section that explains the background. First, the issues of conventional battery and target of the research are discussed. For next generation battery, enhancing both battery performance and safety are important, then thermal stability of each component will need to be improved. To meet these requirements, nanotube materials were focused on that make a sponge-like structure, and a novel battery architecture based on CNT/BNNT was proposed.

Chapter 2 discusses the CNT-based electrode and appropriate properties of CNT. Light-weight electrode which consists of 97 wt% active material and 3 wt% CNT makes battery lighter. However, it had not been discussed in detail what kind of CNT is proper for use. Here, comparison of battery performance was conducted regarding 10 types of CNT. A large length and SSA of CNT helped to make self-supporting electrodes, and large SSA provided superior electrical paths for active material, and it improved performance of positive electrode active material like LCO. On the other hand, a large SSA caused excess electrolyte decomposition in the negative electrode. On $LiCoO_2$-CNT||graphite-CNT cell, specific surface area (SSA) of CNT is critical factor for battery capacity. There was a relationship of irreversible capacity (initial charge capacity–initial discharge capacity) and reversible capacity (initial discharge capacity). The reversible capacity was decreased because Li ion that is transportable between positive and negative electrodes (hereinafter referred to as the active Li) was consumed by the side reaction of reduction decomposition of electrolyte on the negative electrode. Therefore, moderately high SSA is necessary to be a self-supporting electrode, on contrary, it is also important to minimize the consumption of active Li by the side reaction on negative electrode. For these reasons, it was revealed that appropriate SSA of CNT was ~200 $m^2\ g^{-1}$ for obtaining high capacity and ~300 $m^2\ g^{-1}$ for obtaining high-rate performance.

The topic of Chapter 3 is the development of BNNT separator and lightweight and thermally stable nanotube-based architecture. The conventional organic polymer separators have the risk of the serious short-circuit via shrinkage by heat. Here, BNNT that is inorganic but makes flexible sponge structure was focused on. In order to achieving lightweight and thermally stable battery, nanotube-based architecture was developed by using CNT and BNNT for current collector and separator, respectively. The BNNT separator was fabricated by ultrasonication and filtration. Next, thermal stability measurement was conducted by heating the stack of LCO-CNT|BNNT|graphite-CNT at 500 °C under N_2 atmosphere. The BNNT separator did not shrink and the electrical insulation between the positive and negative electrodes were retained after heating. Furthermore, the cell of the heated stack with fresh electrolyte functioned correctly at room temperature. This nanotube-based architecture increased the mass ratio of active materials to total mass of positive and negative electrodes and separator to 93.6%, that is much higher than the value (75%) for the conventional architecture based on metallic foil current collector and organic polymer separator. In this way, light-weight and thermally stable nanotube-based architecture was realized, and this architecture will contribute to enhance energy density and safety of batteries.

Chapter 4 describes batteries based on the nanotube-based architecture that work at high temperature (100–150 °C) for long cycles. $LiFePO_4$ (LFP) and $Li_4Ti_5O_{12}$ (LTO) were used as thermally stable positive and negative electrode active materials, lithium bis(trifluoromethanesulfonyl)imide (LiTFSI) at 1 M as electrolyte salt, and ionic liquid of PP13-TFSI (N-Methyl-N-propylpiperidinium bis(trifluoromethanesulfonyl)amide) was selected as the electrolyte solvent. Half cell of LTO-CNT||Li thick foil (500 μm) showed high Coulombic efficiency (99–100%) and long-term cycle stability > 400 cycles at 100 °C. LFP-CNT||Li (500 μm) also worked for long term, but Coulomb efficiency was not very high (95–99%), and capacity decreased gradually with cycles. Moreover, LFP-CNT||Li (50 and 30 μm) showed a sharp capacity degradation after 220 and 100 cycles, respectively. The degradation was likely caused by the consumption of active Li associated with irreversible reactions. Based on these results, several types of full cells

using two of LFP-CNT, LTO-CNT, or thin Li foil were designed and investigated. The LFP-CNT||LTO-CNT full cell suffered from the depletion of active Li. When areal capacity of LFP was increased by 3 times, cycle stability was improved, however, the excess LFP increased the electrode mass and decreased the energy density. The LFP-CNT||Li full cell realized high voltage and energy density, but has the issues of gradual Li depletion and narrow window for C-rate (~1C). On the other hand, the LTO-CNT||Li full cell showed high Coulombic efficiency and cycle performance even under the condition of small amounts of Li. In addition, the LTO-CNT||Li (50 μm) cell showed repeatable charge/discharge at a quite high temperature of 150 °C for ~200 cycles. Combination of a thin Li foil negative electrode, a CNT-based positive electrode that holds active material with moderate working potential, and the BNNT separator is promising for full cells that work at high temperatures.

Chapter 5 presents summary and perspective of this research. In this thesis, the novel battery structure consisted of electrically conductive and insulate nanotubes was proposed and developed. It was shown that the SSA of CNT influences the self-supporting ability and reversible capacity. And the appropriate properties of CNT for battery application were revealed. Next, BNNT separator and novel battery architecture consisted of CNT and BNNT were proposed and developed. The lightweight property and thermal stability of the battery architecture were demonstrated. This battery structure was realized by self-assembling nanotubes into a nonwoven freestanding membrane through a simple process of dispersion and filtration. Moreover, appropriate condition for improving cycle performance at high temperature operation was examined and discussed. With the nanotube-based architecture and liquid electrolyte, stable charge/discharge for ~200 cycles at 100, 150 °C were achieved with LFP, LTO and thin Li foil.

As described above, this dissertation discusses the advantages of battery architecture based on inorganic nanotubes as well as battery designs with focuses on lightweight, thermal stability, and high-temperature operation.

Chapter 1. Introduction

1.1 Secondary battery

Our life is greatly supported by electricity, and the society has been developing with electricity. In the mass consumption society, the importance of energy storage is getting more important. One of the reasons is to deal with the issues regarding energy resource. Toward the low carbon society, renewable energies (photovoltaic power generation, wind-power generation etc.) will be introduced on a large scale and energy storage plays a major role for stabilizing and leveling of the energy supply. In addition, recently IoT (Internet-of-Things) devices are actively introduced. The secondary battery is also indispensable at this field since energy supply is necessary to drive the remote system like sensor for condition monitoring. Nowadays most of utilities in various places are dependent on electricity. Therefore, if the supply of electricity stopped, we will experience severe confusion. It is also important to prepare the risks of power outage by energy storage system. From these reasons, energy storage and its techniques are indispensable in the now and future society.

Batteries, especially chemical batteries, are the devices that store the electric energy as chemical energy. They are divided into “primary batteries” and “secondary batteries.” The former can only discharge and are used for only one time. On the other hand, the latter one can both charge and discharge repeatedly. Especially lithium-ion batteries are majorly as a consumer use.

Among the secondary (rechargeable) batteries, lithium-ion battery (LIB) has been focused on because it has high energy density. Therefore, the demand is shifted to LIB from nickel-hydrogen battery and lead-acid battery. Energy density indicates the energy per mass or volume (W h kg^{-1} or W h L^{-1}). LIBs have been used in various fields. In a familiar place, they can be found in mobile devices such as PC and smartphone. The world market size will reach to 10 trillion yen in 2021 (prospect), and this value is +57% to previous year. Especially the xEV section showed high ratio to total (78%) and growth (+84% to previous year) [1]. Therefore, the market of LIB has been increasing and the trend continues for a while.

Table 1.1. World market of LIB. Created based on a website [1].

	2021 (billion yen)	Ratio to 2020	2025 (billion yen)	Ratio to 2020
For xEV	8,178	184%	9,389	2.1 times
For small consumer use	1,732	97%	1,846	103%
For ESS/UPS/BTS	603	130%	1,097	2.4 times
Total	10,513	157%	12,332	184%

Here, xEV means the general term of several electric vehicles which are BEV (Battery Electric Vehicle)・HEV (Hybrid Electric Vehicle)・PHEV (Plug-in Hybrid Electric Vehicle)・FCV (Fuel Cell Vehicle). Especially, the demand is concentrated on China. The reasons are analyzed that subsidy policy was prolonged and introduction of EV to public vehicles is actively progressing. Regarding ESS (Energy storage system), UPS (Uninterruptible Power Supply) and BTS (Base Transceiver Station), replacement of lead-acid battery to LIB is progressing especially on ESS since power density is required. The expansion of the whole market is due to the large-scale application such as the vehicles, but the market of small application is also active and growing by the spread of wireless earphones and wearable devices [1].

1.2 Lithium-ion battery

1.2.1 Operation principle

We can obtain electrical energy from the battery by converting chemical energy via a redox reaction. The redox reaction progresses on an oxidant of the positive electrode active material and a reductant of negative electrode active material. This is the reaction of discharge. The secondary battery, in addition, can store energy by the charge (electrolysis, reverse reaction of discharge by applying external force) process. Secondary batteries repeat charge and discharge, then it is important to conduct a highly reversible reaction. The current LIBs utilize the intercalation reaction of lithium-ion. The most notable positive and negative active materials are lithium cobalt oxide ($LiCoO_2$, LCO) and graphite, respectively. Here, I explain the reaction mechanism using this

combination.

Both LCO and graphite have layered structure of planes and Li ion can move easily through the inside. At charging state, Oxidation and reduction reactions are occurs on the positive and negative electrodes, respectively. The Co^{3+} are oxidized to Co^{4+}, then Li^+ is deintercalated (isolates) from LCO due to the charge compensation. On the other hand, when graphite is reduced and negative charge is formed on the carbon, Li^+ is intercalated (enters) between the graphite layers. At discharge process, the contrary reaction occurs. The chemical equations are described as follows. The left side is the discharged state, and the right side is the charged state. In addition, an illustration of the series of reaction are shown in Fig. 1.1.

Positive electrode $\quad LiCoO_2 \rightleftarrows Li_{1-x}CoO_2 + xLi^+ + xe^- \quad (1.1)$

Negative electrode $\quad 6C + xLi^+ + xe^- \rightleftarrows LixC_6 \quad (1.2)$

Whole reaction $\quad 6C + LiCoO_2 \rightleftarrows Li_{1-x}CoO_2 + LixC_6 \quad (1.3)$

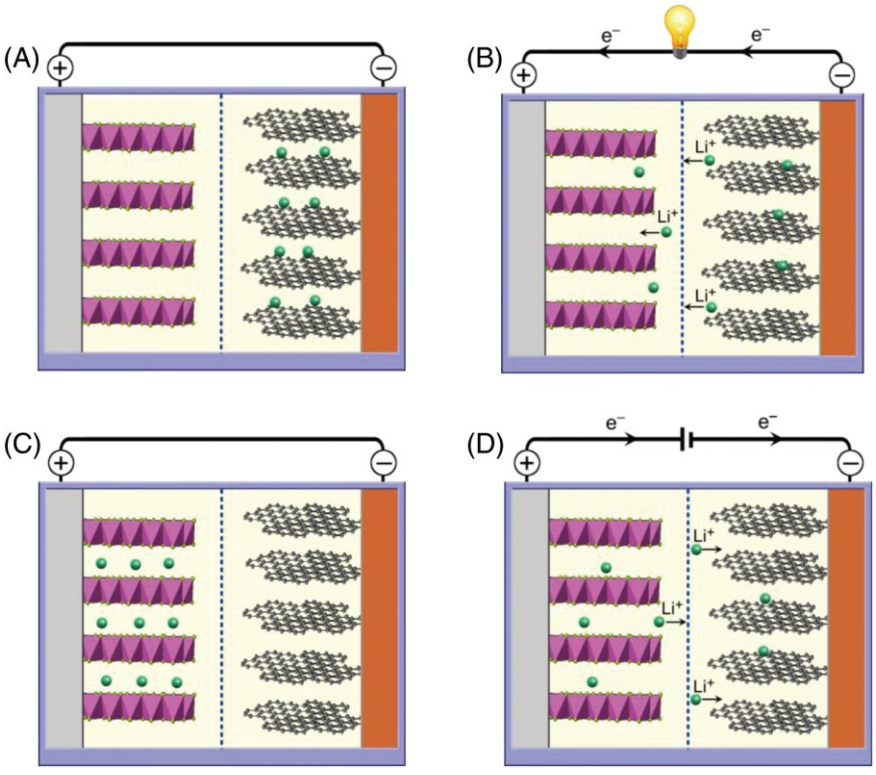

Fig. 1.1. Schematic illustration of LIB in different operational conditions: (A) fully charged state, (B) discharge process, (C) fully discharged state, and (D) charge process. Reproduced from an open access article [2] under the terms of the Creative Commons Attribution License.

1.2.2 Structure of battery

LIB mainly consists of positive and negative electrodes, separator, and electrolyte. The electrodes store Li ion and work as an electrochemical reaction field. The components are active material, binder, conductive additive and metal foil current collector. The active material is an electrochemical reactant with Li ion. Most of active materials are isolated particles and have insufficient electrical conductivity. Therefore, a composite of active material, binder (e.g. PVdF: polyvinylidene difluoride) and conductive additive (e.g. acetylene black) is fabricated and coated on the current collector. Normally metal foil is used as the current collector, and it works as electron path and supporting layer of active material composite. The thickness of current collector is ~10 μm. Al and Cu foils are used for positive electrode and negative electrode, respectively.

The role of the separator is to prevent internal short-circuit by separating positive and negative electrodes spatially without disconnecting ionic transition path. The ion passes through the electrolyte. The separator itself should be electrically insulative and have pores to hold liquid electrolyte. In addition, chemical and thermal stability, flexibility and mechanical strength are required. Representative separator is made of polyolefin such as polyethylene (PE) and polypropylene (PP). These materials are commonplace ones, however, fabricating thin film with microporous structure and high uniformity requires advanced techniques and costs.

Next, several types of cell structure are shown in Fig. 1.2 (A–D). The whole structure, such as the numbers of stacked layers, is different depending on the type, but unit structure is same (Fig. 1.2 E). Every type of these is commercially produced depending on the application. For a prototype study in laboratory, coin shape is often chosen because it is relatively easy to fabricate and evaluate due to its simple structure.

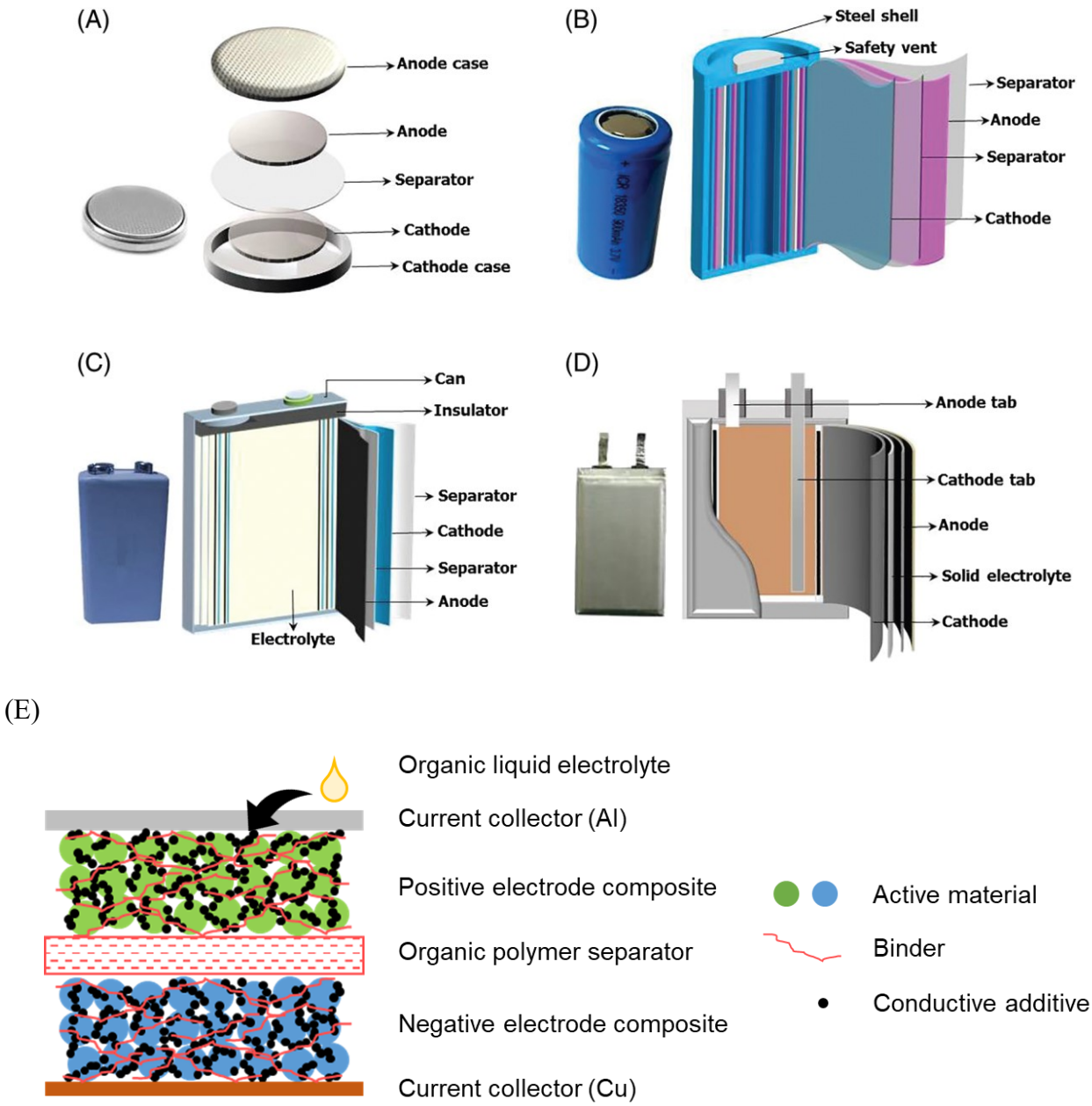

Fig. 1.2. Schematic illustration of typical rechargeable battery configurations (A) coin, (B) cylindrical, (C) prismatic, and (D) pouch shapes. (E) Unit structure. (A–D): Reproduced from an open access article [2] under the terms of the Creative Commons Attribution License.

1.2.3 Energy density of lithium-ion battery

One of the most important advantages of LIB is its high energy density. The value is especially high compared to other secondary batteries (Fig. 1.3).

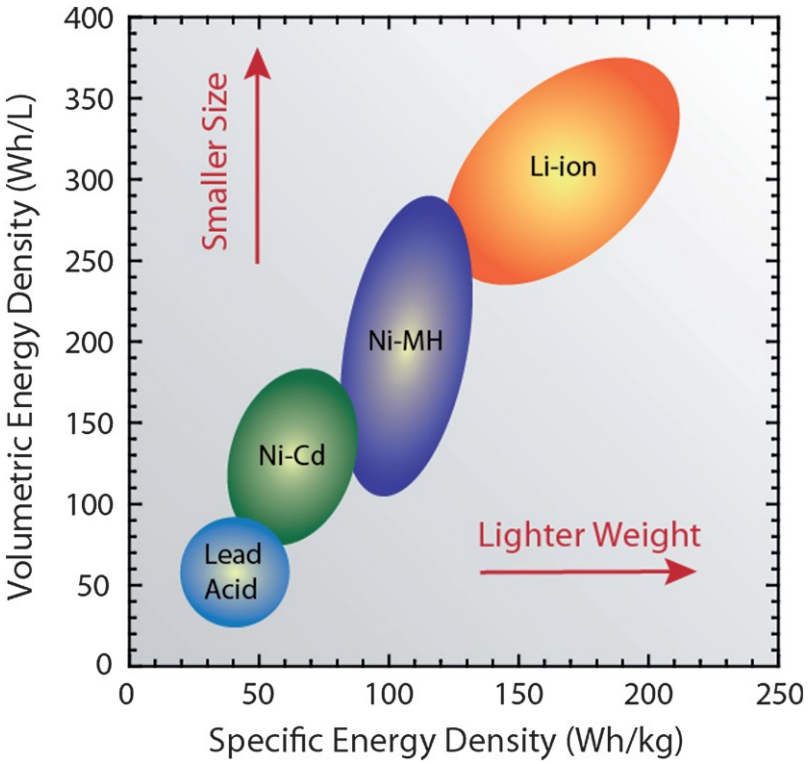

Fig. 1.3. Energy density of representative secondary battery. Reproduced with permission of Royal Society of Chemistry from [3]; permission conveyed through Copyright Clearance Center, Inc.

One of the reasons is the voltage of battery. High voltage contributes to increase energy density since energy density is proportional to voltage and capacity. LIB has high discharge voltage of ~4 V. This value is 2–3 times higher than lead-acid battery (~2 V) and Ni-Cd, Ni-H battery (~1.3 V). This is because of the wide potential window of the organic liquid electrolyte. The aqueous electrolyte is easily decomposed at ~4V that value is much larger than theoretical decomposition voltage of 1.23 V, but the organic liquid electrolyte used in LIB can endure such high voltage.

However, the energy density is still small depending on use, like xEV. Therefore, various scientific and engineering research and improvement are conducted, and the energy density of commercial LIB increases year by year (Fig. 1.4) [4].

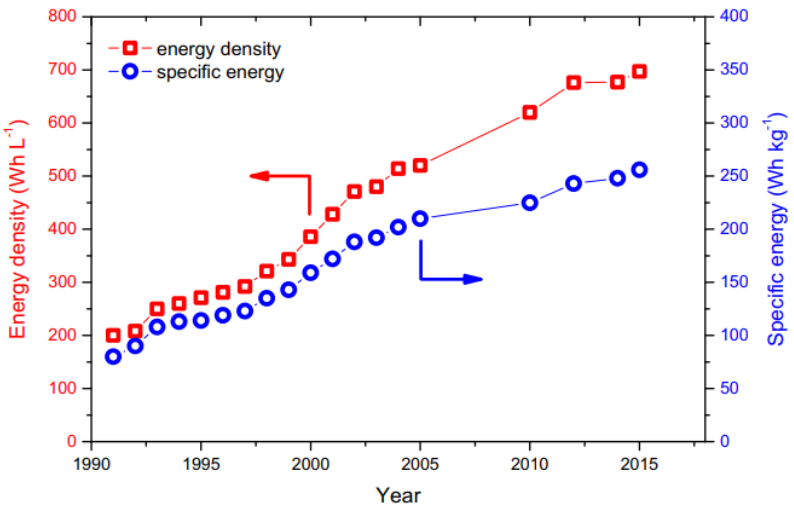

Fig. 1.4. Transition of energy density per cell. Reproduced from [4] with permission from Springer Nature.

1.3 Safety and thermal stability of LIB

As stated before, the demand for energy density is increasing year by year. Increase of the energy density enhance the convenience, however, thermal management and the risk of the accident become severe in that case. Table. 1.2 shows the accidents due to LIB that happened in the past few years.

Table. 1.2. Fire and explosion accidents of LIB in the past few years. Created based on an article [5].

Date	Accident	Cause
Jan 2013, Jan 2014	Three fire accidents of Boeing 747, happened in Boston, America, Takamatsu and Tokyo, Japan	Internal short circuit of the LIBs and the failure of the battery management system (BMS)
April 2015	EV bus caught fire during charge, Shenzhen, China	Overcharge of the battery due to the failure of BMS
31 May 2016	The storage room of the LIB caught explosion, Jiangsu, China	Caused by the fully charged LIBs, maybe self-ignition
16 May 2017	Panasonic announced to recall over 270 thousand LIBs	Potential overheating and fire accidents
January 2018	4 MW/12 MWh energy storage system (ESS) caught fire and explosion, Korea	One LIB caught fire and propagated to over 3500 LIBs

There are several safety mechanisms of current protection device. Shutdown function of separator (internal), PTC (Positive Temperature Coefficient) thermistor (external) are the representatives. The safety of the LIB is said to be fundamentally high, however, it is impossible to

prevent troubles perfectly. Actually, some several accidents are reported every year. There is a possibility of causing fatal accident by the failure of the battery depending on the situations, like in a large-scale operation or an unsuitable usage. Therefore, safety should be also highly valued as same as the battery performance. Fundamental improvement is desired not to reach to serious accident like ignition and explosion.

Related to the safety issue, operation temperature should be considered. As previously stated, xEV, small consumer use, and ESS/UPS/BTS are the general uses of LIB and have the majority of the market, but special uses are also demanded by specific fields. Present LIBs are designed to work at < 60 °C. If they can operate at higher temperatures, they will find applications in various fields such as oil drilling, space exploration, and high-temperature device monitoring [6,7]. In addition, different from portable use, the operation temperature of large-scale use such as EV does not have to be room temperature.

However, it is difficult to conduct long-term stable charge and discharge > 60 °C because there is a risk of causing the series of reactions as follows [5,8].

1. Breakdown of SEI: Solid electrolyte interphase (a kind of protection layer) > 70 °C
2. Reaction between negative electrode and electrolyte > 100 °C
3. Internal short-circuit by shrinkage or melt of separator > 130 °C for PE and > 165 °C for PP
4. Decomposition of electrolyte > 200 °C
5. Reaction between positive electrode and electrolyte > 300 °C
6. Decomposition of positive electrode and oxygen release (depends on metal species)

The thermal stability of the positive electrode active material differs by the metal species of layered metal oxide. In the organic liquid solvent, the onset temperature for self-sustained exothermic reaction is 150, 220 and 310 °C for $LiCoO_2$, $Li(Ni_{0.1}Co_{0.8}Mn_{0.1})O_2$ and $LiFePO_4$ (all charged to 4.2 V vs Li metal), respectively [5].

1.4 Target and objective of this research

Based on the above contents, here I discuss the target and objective of this research with reviewing the conventional battery structure.

Energy density of the LIB is steadily increasing. However, LIB easily becomes to be high temperature at the use of high capacity or large-scale battery. Therefore, it is getting more difficult and important to keep the safety.

Preferably, properly high temperature is suitable to radiate the heat that is generated while charge and discharge, since the heat radiation is proportional to the temperature difference between radiator and environment. At the same time, improvement of energy density per module would be possible. Normally thermal management is necessary such as cooling system or making a space between the battery modules [9,10], however, these managements increase the mass or volume for a lot. If they are simplified, energy density per module will increase significantly. Moreover, high-rate performance (quick charge and discharge) is expected at high temperature because reaction on the electrodes and diffusion of Li ion is promoted.

Therefore, it is necessary to develop the battery with minimum amount and thermally stable materials. In this research, nanotubes that make sponge-like structure are focused on and the light-weight and thermally stable battery architecture was proposed and developed. Moreover, high temperature operation > 100 °C was conducted with the nanotube-based architecture.

1.4.1 Improvement of the energy density by the optimization of the electrode structure

The LIB electrodes consist of not only active material but also supporting materials of current collector, binder and conductive additive. The mass of these supporting materials is not small. To obtain high energy density as a device, it is necessary to consider energy density per electrode, moreover, per cell. **Fig. 1.** Fig 1.5 shows the mass ratio on the commercial cylindrical cell of NCR18650B at the level of positive and negative electrodes, separator and electrolyte. This figure was fabricated by the calculation from the literature [11].

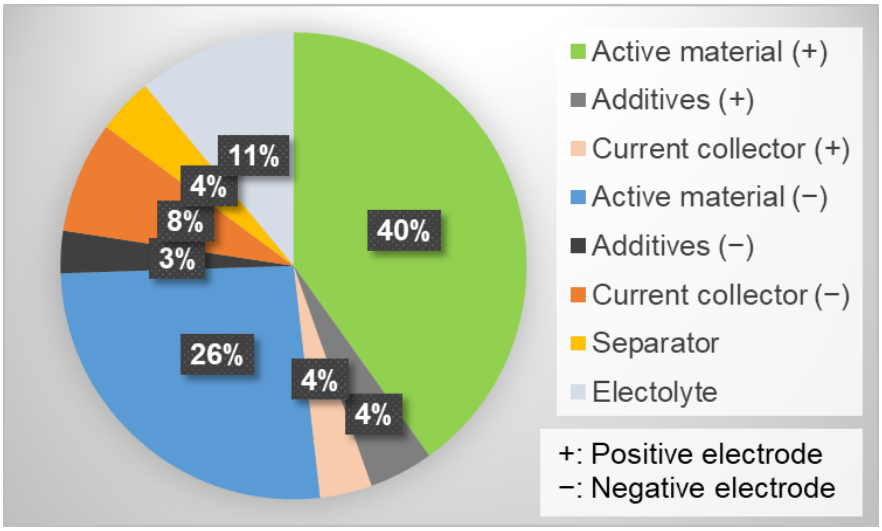

Fig. 1.5. Mass ratio on the cylindrical cell of NCR18650B, calculated from [11]

To obtain high energy density, the elimination of non-capacitive components is effective. Therefore, electrodes based on 1 mass% 3D current collector of submillimeter-long few-wall carbon nanotube (CNT) that held 99 mass% active materials were developed (Fig. 1.6) [12]. Here, the CNT played the roles of the binder, conductive filler, and current collector.

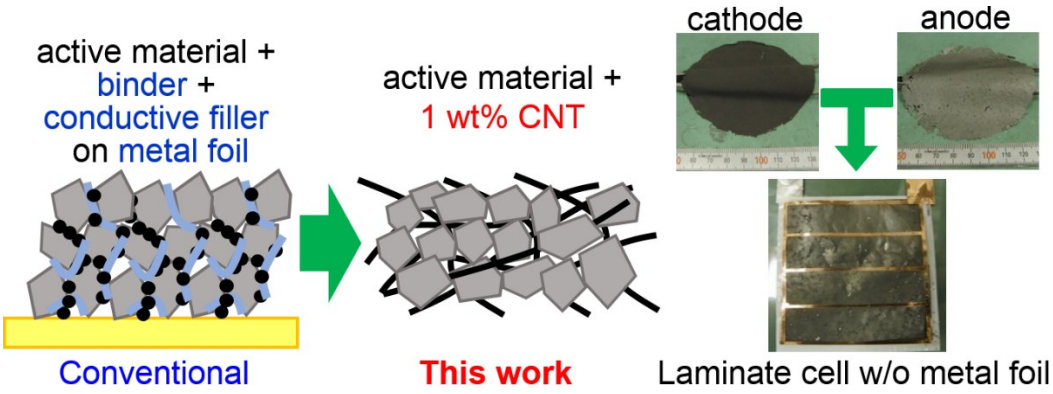

Fig. 1.6. Active material-CNT composite. Reproduced from [12] with permission from Elsevier.

CNT is a tube-like structure nanomaterial consists of carbon atoms. CNT has a rounded structure of graphene. Nanotubes are classified by the number of concentric cylinders, that is called wall number, like single-wall carbon nanotube: SWCNT, few-wall carbon nanotube: FWCNT, and multi-wall carbon nanotube: MWCNT.

CNT enhances not only the conductivity to out-plane but also to in-plane, it is possible to achieve long-distance electron transport with small amount of metal foil. Fig. 1.7 shows the laminate cell with CNT-based electrodes and comb-shaped metal foil. The laminate cell showed similar rate performance and cycle performance though the mass of metal foil was 14% of the 10 μm-thick metal foil. Therefore, the combination of the CNT 3-dementional current collector and comb-shaped metal foil is effective to increase energy density by eliminating the supporting materials as much as possible.

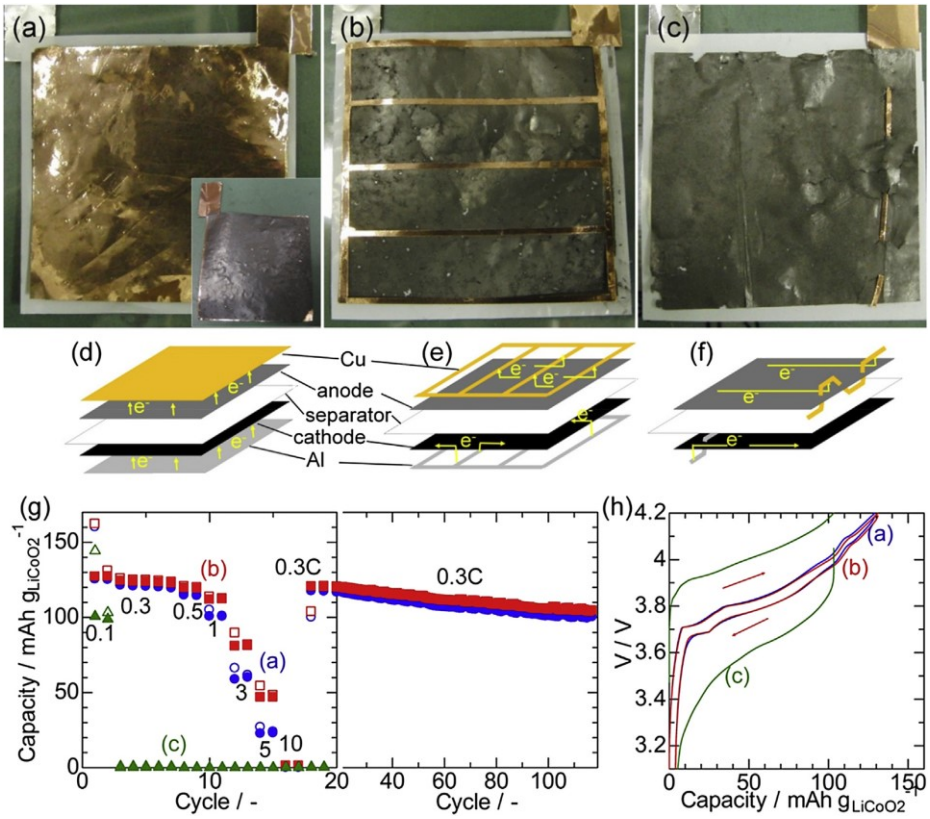

Fig. 1.7. (a–c) Laminate cell assemblies of Cu/graphite-1 wt% CNT/separator/$LiCoO_2$-1 wt% CNT/Al with: (a) Metal foils in full contact with the electrodes, (b) metal combs (1-mmwide wires with 10-mm-wide spaces) in partial contact with the electrodes, and 1-mm-wide wire sewn into one of the edges of the electrodes (c) (electrolyte: 1 M $LiPF_6$ in 1:1 v/v EC/DEC). (d–f) Schematics of the cell assemblies in (a–c). (g) Charge–discharge capacities of the cells at 0.1C, 0.3C, 0.5C, 1C, 3C, 5C, 10C, and 0.3C. (h) Charge–discharge curve at the second cycle (0.1C). Reproduced from [12] with permission from Elsevier.

The metal-foil free CNT-based electrodes were developed, however, only one type of CNT was considered. In this research, the effects of the structural properties of CNT on the battery performance were considered by using 10 types of CNT that have different SSA, length, etc. These topics are discussed in Chapter 2.

1.4.2 Battery architecture consist of CNT and BNNT

To develop batteries that have high safety and high energy density, the selection of the separator becomes crucially important since it prevents the direct contact and runaway reaction between the negative and positive electrodes. The melting point of the present polymer separators are said to be low, then they have both advantage and disadvantage about safety.

The advantage is the shutdown function that works as a safety mechanism. When the temperature of the battery accidentally increased to near the melting point of separator, the micropores of separator close by heat and the transportation of ions was shut out. This phenomenon can be measured as an increase of electrical resistance. This mechanism is said to be effective to stop the abnormal fever. However, if the temperature increase continued after shutdown, the polymer separator itself will shrink significantly (Fig. 1.8). This is the very serious problem since it will soon cause direct internal short-circuit by touching the positive and negative electrodes. Therefore, thermally stable separator that never shrinks > 200 °C is demanded. Various studies have been conducted to address this issue. Typical examples are ceramic coating on the polyolefin separator, but there is a limitation of thermal stability while using the organic materials for the main constituent.

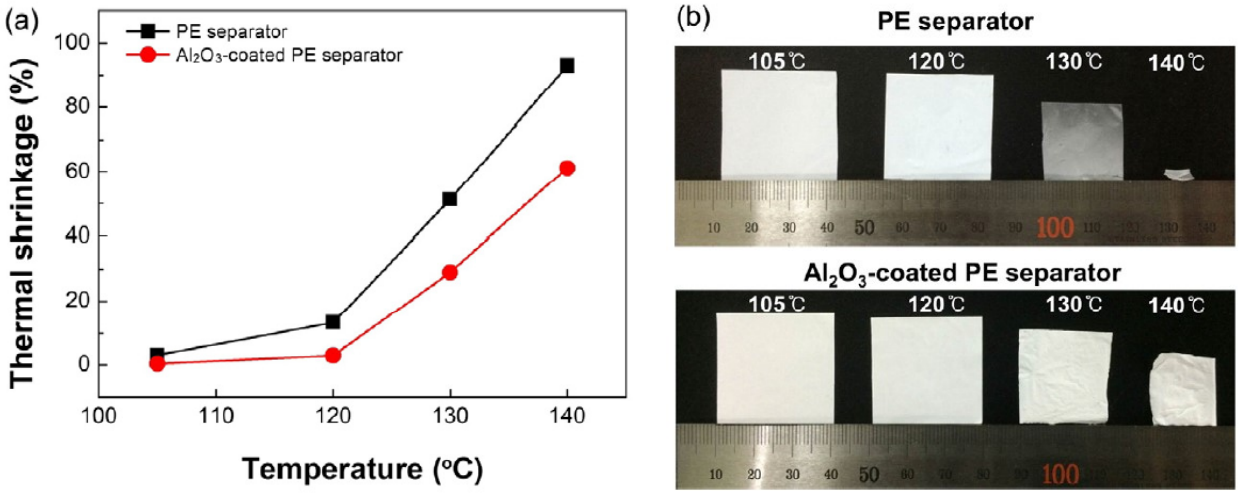

Fig. 1.8. (a) Thermal shrinkage of a PE separator and an Al_2O_3-coated PE separator. (b) photographs of the PE separator and the Al_2O_3-coated PE separator. Reproduced from [13] with permission from Elsevier.

In this research, an investigation about the boron nitride nanotube (BNNT) separator that is light-weight and has high thermal stability was conducted. In addition, nanotube-based architecture was proposed and developed that consists of with CNT-based electrodes and BNNT separator, which makes battery lighter and safer.

BNNT consists of boron and nitrogen atoms, and it has tube-like structure (Fig. 1.9). The structure is similar to CNT, but in contrast to CNT, BNNT is white and electrically insulative. Moreover, BNNT has high thermal stability that can endure 900 °C in air atmosphere [14,15]. Therefore, BNNT is expected to show good formability as a paper and excellent thermal stability in the battery use.

(a) (b) (c)

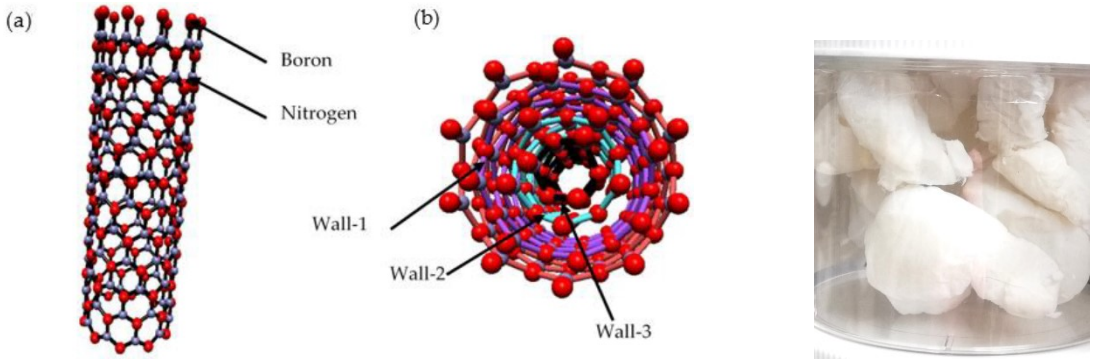

Fig. 1.9. Structure of (a) BNNT. (b) Multi-wall BNNT. (c) Appearance of BNNT. (a,b): Reproduced from an open access article [16] under the terms of the Creative Commons Attribution License.

The examinations were conducted with single BNNT separator on the idea that it had not better to have the shutdown function. This is because there is a plan of conducting high temperature operation > 100 °C in this research, then the shutdown function is not suitable at that time. If the shutdown function is demanded, the only thing to do for giving the function is to stack a sheet of polyolefin (like PP) separator to the BNNT paper. The BNNT/PP separator would show shutdown function by PP, and it is possible to prevent direct short-circuit of positive and negative electrodes by BNNT if the shrinkage of polymer occurs. The novel battery architecture based on CNT and BNNT is discussed in Chapter 3.

1.4.3 High temperature operation of secondary battery

It is difficult to conduct charge/discharge of conventional LIB over 60 °C since the organic materials in the conventional battery are weak to heat, and side reaction is promoted. The negative effects caused at high temperature are as follows.

Electrodes

→ Side reaction with electrolyte

→ Decrease of connecting force of binder ・・・ Detachment of active material from current collector

Separator

→ Shrinking, Melting

Electrolyte

e.g. Solvent of ethylene carbonate and diethyl carbonate, supporting electrolyte salt of $LiPF_6$

→ Volatilization of solvent, decomposition of solvent and supporting electrolyte salt

Thermally stable electrodes and separator were considered in Chapter 3 by developing the CNT/BNNT architecture. Therefore, the remaining issue about individual components is the electrolyte. The organic liquid solvents in the conventional electrolytes are not appropriate for high temperature operation because they are volatile and flammable. In this study, the ionic liquid (IL) is used for electrolyte solvent. IL is also called "room temperature molten salt," and its vapor pressure is quite low though it is liquid state. Therefore, IL is considered suitable for high temperature operation since it is non-volatile, non-flammable and highly stable to heat.

There are a lot of research using liquid electrolyte for battery application. However, high temperature operation on nanotube-based architecture is highly novel. In this study, the following points were discussed in Chapter 4: what causes the performance deterioration at high temperature operation, what charge/discharge condition is appropriate, and which combination of active materials is suitable for obtaining good cycle performance and energy density.

1.5 Summary

The energy density of LIBs continues to increase, but at the same time, LIBs are becoming easier to be high temperature due to the increased heat generation and lower heat dissipation efficiency associated with larger capacities and larger sizes. LIBs are weak to heat, and large modules require space for heat dissipation or the introduction of cooling mechanisms. Then the energy density is severely limited. Therefore, thermal stability is essential for high energy density and safety.

To obtain both high energy density and thermal stability, it would be necessary to alternate the

battery components drastically. The LIB consists of two electrodes, a separator, and an electrolyte. Conventional electrodes are fabricated by applying a mixture of active materials, conductive materials, and organic polymer binders on a metal foil current collector. However, the mass ratio of materials other than positive and negative electrode active materials is large, and many heat-sensitive materials such as organic polymer separators and organic electrolyte are used. Hence, conventional architecture has limitation in energy density and thermal stability. Therefore, it is appropriate to construct batteries with a minimum amount of non-capacitive materials and replace heat-sensitive materials with thermally stable ones. In this study, the inorganic nanotubes were focused on that are thermally stable, lightweight, and yield self-supporting sponge-like structure, and a novel battery architecture was proposed for improved energy density and thermal stability.

References

[1] 富士経済, “リチウムイオン二次電池の世界市場を調査 PRESS RELEASE,” (Online) https://www.fuji-keizai.co.jp/file.html?dir=press&file=22050.pdf&nocache, (Accessed: 2022/11/20).

[2] Y. Liang, C. Z. Zhao, H. Yuan, Y. Chen, W. Zhang, J. Q. Huang, D. Yu, Y. Liu, M. M. Titirici, Y. L. Chueh, H. Yu, Q. Zhang, A review of rechargeable batteries for portable electronic devices, InfoMat. 1 (2019) 6–32.

[3] B. J. Landi, M. J. Ganter, C. D. Cress, R. A. DiLeo, R. P. Raffaelle, Carbon nanotubes for lithium ion batteries, Energy Environ. Sci. 2 (2009) 638–654.

[4] T. Placke, R. Kloepsch, S. Dühnen and M. Winter, “Lithium ion, lithium metal, and alternative rechargeable battery technologies: the odyssey for high energy density,” J. Solid State Electrochem., vol. 21, p.1939, 2017.

[5] Q. Wang, B. Mao, S. I. Stoliarov, J. Sun, A review of lithium ion battery failure mechanisms and fire prevention strategies, Progress in Energy and Combustion Science 73 (2019) 95–131.

[6] F. Mestre-Aizpurua, S. Hamelet, C. Masquelier, M.R. Palacín, High temperature electrochemical performance of nanosized LiFePO4, J. Power Sources 195 (2010) 6897–6901.

[7] D.E. Glass, J.-P. Jones, A.V. Shevade, D. Bhakta, E. Raub, R. Sim, et al., High temperature primary battery for Venus surface missions, J. Power Sources 449 (2020) 227492.

[8] X. Feng, M. Ouyan, X. Liu, L. Lu, Y. Xia, X. He, Thermal runaway mechanism of lithium ion

battery for electric vehicles: A review, Energy Storage Materials 10 (2018) 246–267.

[9] S. Shahid, M. Agelin-Chaab, A review of thermal runaway prevention and mitigation strategies for lithium-ion batteries, Energy Conversion and Management: X 16 (2022) 100310.

[10] R. D. McKerracher, J. G.-Guemez, R. G. A. Wills, S. M. Sharkh, D. Kramer, Advances in Prevention of Thermal Runaway in Lithium-Ion Batteries, Adv. Energy Sustainability Res. 2 (2021) 2000059.

[11] M. Hagen, D. Hanselmann, K. Ahlbrecht, R. Maça, D. Gerber, J. Tübke, Lithium–Sulfur Cells: The Gap between the State-of-the-Art and the Requirements for High Energy Battery Cells, Adv. Energy Mater. 5 (2015) 1401986–1401996.

[12] K. Hasegawa, S. Noda, Lithium ion batteries made of electrodes with 99 wt% active materials and 1 wt% carbon nanotubes without binder or metal foils, J. Power Sources 321 (2016) 155–162.

[13] D. W. Lee, S. H. Lee, Y. N. Kim, J. M. Oh, Preparation of a high-purity ultrafine α-Al2O3 powder and characterization of an Al2O3-coated PE separator for lithium-ion batteries, Powder Technology 320 (2017) 125–132.

[14] Y. Chen, J. Zou, S. J. Campbell, and G. L. Caer, Boron nitride nanotubes: Pronounced resistance to oxidation. Appl. Phys. Lett. 84 (2004) 2430–2432.

[15] K. S. Kim et al., Polymer nanocomposites from free-standing, macroscopic boron nitride nanotube assemblies, RSC Adv. 5 (2015) 41186–41192.

[16] A. B. Kakarla, I. Kong, In Vitro and In Vivo Cytotoxicity of Boron Nitride Nanotubes: A Systematic Review, Nanomaterials 12 (2022) 2069–2110.

Chapter 2. CNT-based electrode and appropriate properties of CNT

The content of this Chapter has been published in: K. Kaneko, M. Li and S. Noda*, "Appropriate properties of carbon nanotubes for the three-dimensional current collector in lithium-ion batteries," Carbon Trends 10, 100245–100252 (2023). DOI: 10.1016/j.cartre.2022.100245

2.1 Objective

Secondary batteries with high energy density and long lifetimes are necessary to satisfy increasing demands for electric energy storage applications, such as electric vehicles, 5G base stations, and the Internet of Things [1–4]. To achieve high energy density, optimization of the cell structure is as important as the development of active materials. In conventional lithium-ion battery (LIB) electrodes, the active material and conductive additive are coated and fixed onto the current collector using polymeric binders. Metal foils are essential in this conventional architecture, to serve as the current collector that carries electrons for the electrode reactions and as a substrate for slurry applications; however, metal foils are still relatively heavy, which increases the mass and decreases the energy density of cells [5].

Various carbon materials have been used as conductive additives in conventional LIB architectures. Among these, carbon nanotubes (CNTs) and graphene can yield self-supporting, sponge-like paper structures, enabling an alternative three-dimensional (3D) architecture for the electrodes, without using metal foils or polymeric binders [6–11]. In particular, long (> 100 μm) and thin (~10 nm or less) CNTs can be used for self-supporting electrodes with content as low as 1 mass%, owing to their large aspect ratio [8]; in contrast, graphene requires a minimum content of 20 mass% [9–11]. Submillimeter-long CNTs with only a few walls have been used in such self-supporting electrodes, where the CNTs played multiple roles, as the binder, conductive filler, and current collector, enhancing the mass fraction of the active materials and enabling stable charge-discharge cycles of a pouch cell (50 mm × 50 mm) with a support of lightweight combs instead of heavy foils of metal [8].

The CNT-based electrode architecture has been effective for conventional active materials, such as graphite for the negative electrode and lithium cobalt oxide (LCO) for the positive electrode [8,12], and emerging high-capacity active materials such as silicon [13–15] and sulfur [15–18]. A CNT-based sulfur positive electrode showed high performance because of its enhanced electrical conduction pathways and high gravimetric and volumetric capacities attributed to the lightweight and flexible nature of the porous CNT sponge [16]; however, a CNT-based silicon negative electrode provided low Coulombic efficiency because of electrolyte decomposition and low volumetric capacity, which were attributed to the highly porous structure [15,16]. Thus, it is important to select a CNT matrix with the appropriate structural properties; however, most studies have only examined one type of CNT. Previously both single- and multi-wall CNTs were investigated, but the structural properties, such as the number of walls and specific surface area (SSA), were not clarified [8]. Because multi-wall CNTs exhibit a wide variety in their structures, with wall numbers ranging from 2 to >100, diameters from ~2 nm to > 100 nm, and lengths from submicrometer to multiple millimeters, examining the effects of these properties on electrode performance is essential to extract the full potential of the CNT-based electrode architecture.

In this work, a graphite-CNT negative electrode and an LCO-CNT positive electrode were fabricated using ten different CNTs with various SSAs (187–960 m^2 g^{-1}) and lengths (26–270 μm) (Table 2.1 and Fig. 2.1). Half and full cells were made using these electrodes, and the electrode/battery performances were evaluated. We clarified the requirements for making self-supporting electrodes at a low CNT content of 3 mass% and the appropriate structural properties required to achieve high discharge capacity, Coulombic efficiency, and rate performance.

Table 2.1. SSA and length of CNTs used in this research.

CNT	SSA (m^2 g^{-1})	Length (μm)	Conductivity of paper (S cm^{-1})	Average diameter (nm)
A	187	114	53	14
B	240	183	54	11
C	287	174	48	-
D	498	53	1.6	-
E	501	226	46	8
F	793	56	7.3	-
G	768	270	24	-
H	840	26	6.0	-
I	864	121	12	-
J	960	59	7.2	5

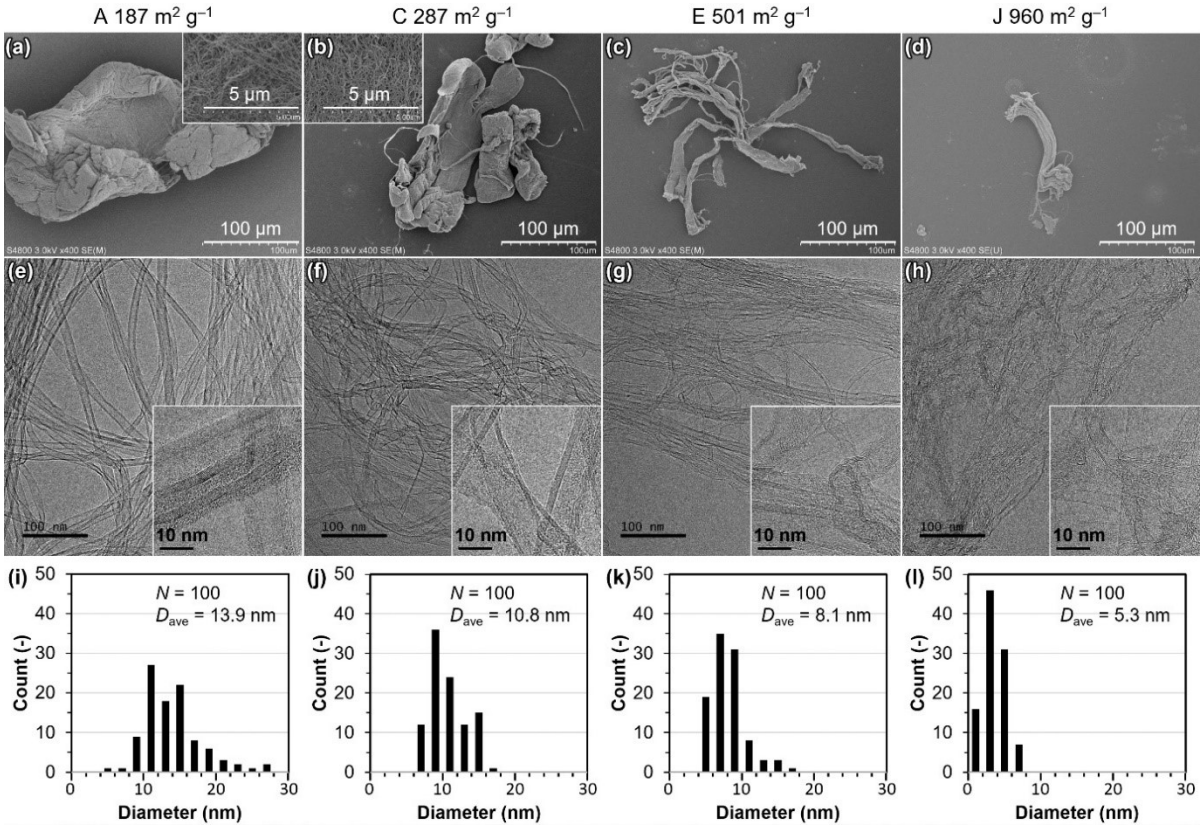

Fig. 2.1. Structure of representative CNTs used in this work. (a–d) SEM images of the CNT bundles, as separated from the ceramic support beads. (e–h) TEM images of the CNTs. (i–l) Diameter distributions of the CNTs determined by TEM. CNT types are A (a, e, and i), C (b, f, and j), E (c, g, and k), and J (d, h, and l).

2.2 Experimental

2.2.1 Fabrication of graphite-CNT and LCO-CNT electrodes

Ten types of CNTs were synthesized on spherical ceramic beads by fluidized-bed chemical vapor deposition [19–21] and used herein. The CNTs were separated from the ceramic beads by shaking the beads in a sealed bottle, and then they were characterized using a scanning electron microscope (SEM; Hitachi S-4800, Tokyo, Japan). The CNTs were also transferred to a microgrid and characterized using a high-resolution transmission electron microscope (HR-TEM; JEOL JEM-2100, Akishima, Japan). The diameters were measured for one hundred CNTs from each sample type to obtain the diameter distributions and average diameters. The results are summarized for four representative CNTs (A, C, E, and J) in Fig. 2.1. SSA was measured by nitrogen gas adsorption (BELSORP-mini II, MicrotracBEL Corp., Osaka, Japan), which ranged from 187 m^2 g^{-1} (CNT A) to 960 m^2 g^{-1} (CNT J), as shown in Table 2.1 Self-supporting CNT-based electrodes were fabricated by co-dispersing and filtering the CNTs and active materials, following our previous report [8]. The CNTs and graphite (natural graphite; SEC Carbon, Amagasaki, Japan) or LCO (TOSHIMA Manufacturing, Higashi-Matsuyama, Japan) were weighed out in a 3:97 mass ratio. The bundled CNTs and grains of active material were co-dispersed in 2-propanol by sonication (bath-type VS-50R, VELVO-CLEAR, Tokyo, Japan) for 10 min. Then, the dispersed solution was vacuum-filtered on a polytetrafluoroethylene membrane filter (Merck Millipore, Burlington, MA, USA) to fabricate conductive self-supporting paper-like films. The papers were vacuum-dried at 120°C for ≥ 2 h to remove the solvent. The negative and positive electrodes were fabricated using circular papers of 11–12 mm in diameter with a designed areal capacity of 1.0 mA h cm^{-2} (372 mA h g^{-1} and 2.7 mg cm^{-2} for graphite; 137 mA h g^{-1} and 7.3 mg cm^{-2} for LCO). The microstructures of the CNT-based electrodes were observed using SEM.

2.2.2 Charge-discharge measurement

Battery cells (2032-type coin cells) were assembled in an Ar-filled glove box (H_2O and O_2 below

1 ppmv; UNICO, Moriya, Japan). Full cells were assembled with a graphite-CNT negative electrode, LCO-CNT positive electrode, polypropylene separator, and electrolyte comprised of 1 M $LiPF_6$ (Kishida Chemical, Osaka, Japan) in ethylene carbonate and diethyl carbonate (v:v = 1:1) (EC:DEC; Kishida Chemical, Osaka, Japan). The negative-to-positive capacity ratio was approximately 1. For the half cells, a lithium foil (500 μm thick, 12 mm φ; Honjo Chemical, Osaka, Japan) was used as the counter electrode. Galvanostatic charge-discharge was performed using a charge-discharge system (Hokuto Denko, Tokyo, Japan) in the voltage range of 3.0–4.2 V for graphite/LCO and LCO/Li, and 0–2.5 V for graphite/Li. To evaluate rate performance, charge-discharge tests were performed by alternating the current density between 0.1 and 10 mA cm^{-2} every five cycles. To evaluate cycle performance, charge-discharge tests were performed for ≥ 300 cycles at 0.3 mA cm^{-2} after an initial cycle at 0.1 mA cm^{-2}.

2.3 Results and discussion

2.3.1 Structural and physical properties of graphite-CNT and LCO-CNT electrodes

Fabrication of the graphite-CNT and LCO-CNT electrodes is illustrated in Fig. 2.2a. As shown in Fig. 2.2b, self-supporting papers were fabricated with only 3 mass% of CNTs using a simple ultrasonication-filtration method. Such self-supporting papers can only be made using CNTs with diameters of ~10 nm or less, and cannot be made of CNTs or carbon fibers with larger diameters, even at a concentration as high as 10 mass% [8]. All CNTs (SSAs of 187–960 $m^2\ g^{-1}$ and lengths of 30–300 μm) yielded self-supporting films without using polymeric binders, except type D, which had a moderate SSA (498 $m^2\ g^{-1}$) and small length (53.4 μm) (Table 2.1). Even if the CNT length was short, a large SSA assisted the self-supporting ability (type H: 25.7 μm, 840 $m^2\ g^{-1}$), and the opposite was also true (type A: 114 μm, 187 $m^2\ g^{-1}$). The CNT should have a sufficient length (several 10 μm or more), in addition to a small diameter (~10 nm or less), to form a self-supporting paper.

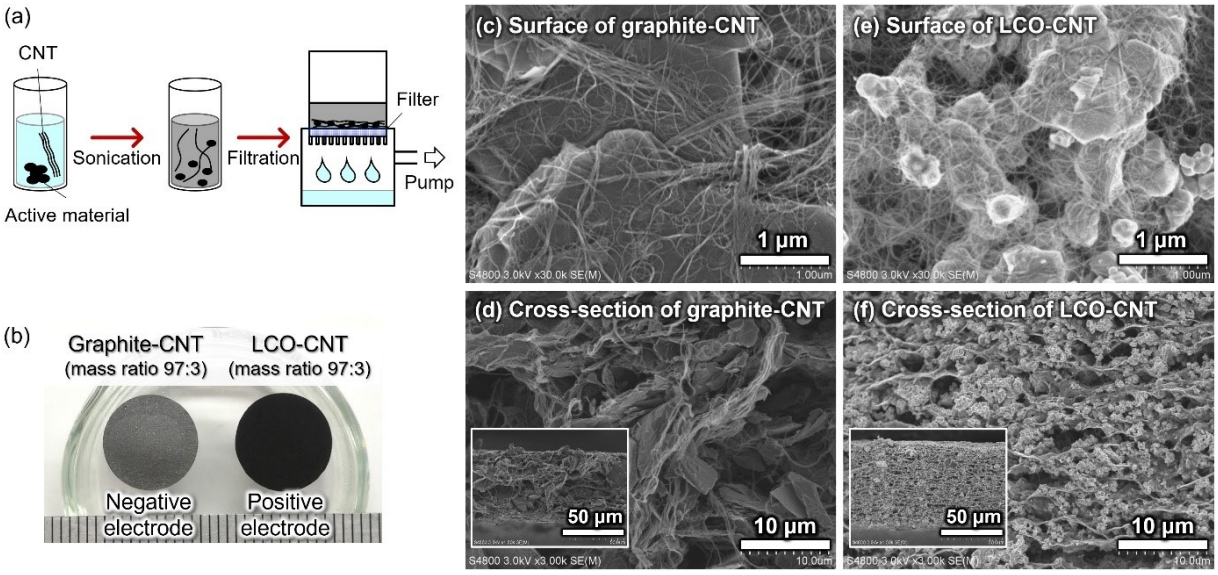

Fig. 2.2. CNT-based LIB electrodes. (a) Illustration of the fabrication process. (b) Photograph of graphite-CNT and LCO-CNT electrodes. (c–f) SEM images of graphite-CNT and LCO-CNT with a CNT SSA of 501 $m^2\ g^{-1}$.

2.3.2 Initial charge-discharge performance of graphite-CNT and LCO-CNT electrodes and their half and full cells

The battery performances of the 2032-type coin cells comprised of CNT-based electrodes were evaluated using charge and discharge measurements. The negative and positive electrodes were prepared with an areal capacity of 1 mA h cm^{-2} (372 mA h g^{-1} and 2.7 mg cm^{-2} for graphite; 137 mA h g^{-1} and 7.3 mg cm^{-2} for LCO). Individual electrodes had slightly different areal masses, so the discharge capacity was shown relative to the LCO mass (g_{LCO}) for the LCO/Li half cell and graphite/LCO full cell and relative to the graphite mass (g_{gr}) for the graphite/Li half cell. Fig. 2.3 shows the cycle and rate performance of the LCO/Li half cells. The half cells showed a lithiation capacity close to the theoretical capacity for LCO (137 mA h g_{LCO}^{-1}) at a low current density of 0.1 mA cm^{-2}, which stayed high for 0.2–1 mA cm^{-2}, then decreased for 2–10 mA cm^{-2}. The capacities were similar among different CNTs at low current densities (0.1–1 mA cm^{-2}) but were significantly different at high current densities (1–10 mA cm^{-2}). After returning to the current density of 0.1 mA cm^{-2}, the capacity returned to ~120 mA h g_{LCO}^{-1} and gradually decreased during cycling (Fig. 2.3a).

The delithiation-lithiation curves at 0.1 mA cm^{-2} show a wide plateau at ~3.9 V vs. Li, revealing the high availability of electrical pathways to LCO particles for all nine CNTs with SSAs of 187–960 m^2 g^{-1} (Fig. 2.3b). At the moderate current density of 1 mA cm^{-2}, the plateau became reduced, especially for the type A CNT with a SSA of 187 m^2 g^{-1} (Fig. 2.3c). At the high current density of 5 mA cm^{-2}, the difference became clearer, showing improved charging rate performance for CNTs with larger SSAs (Fig. 2.3d). Because the pure papers made of CNTs with small SSAs (187–287 m^2 g^{-1}) showed high conductivities of ~50 S cm^{-1} (types A, B, and C in Table 2.1) and pure papers made of CNTs with large SSAs (840–960 m^2 g^{-1}) showed lower conductivities of 6–12 S cm^{-1} (types H, I, and J), electrical conduction through the LCO-CNT films should be sufficiently high for all nine CNTs. The contact area between the CNTs and the LCO particles should be proportional to the SSA of CNTs, and therefore the bottleneck should be the electrical conduction between the CNTs and the LCO particles for LCO at high current densities.

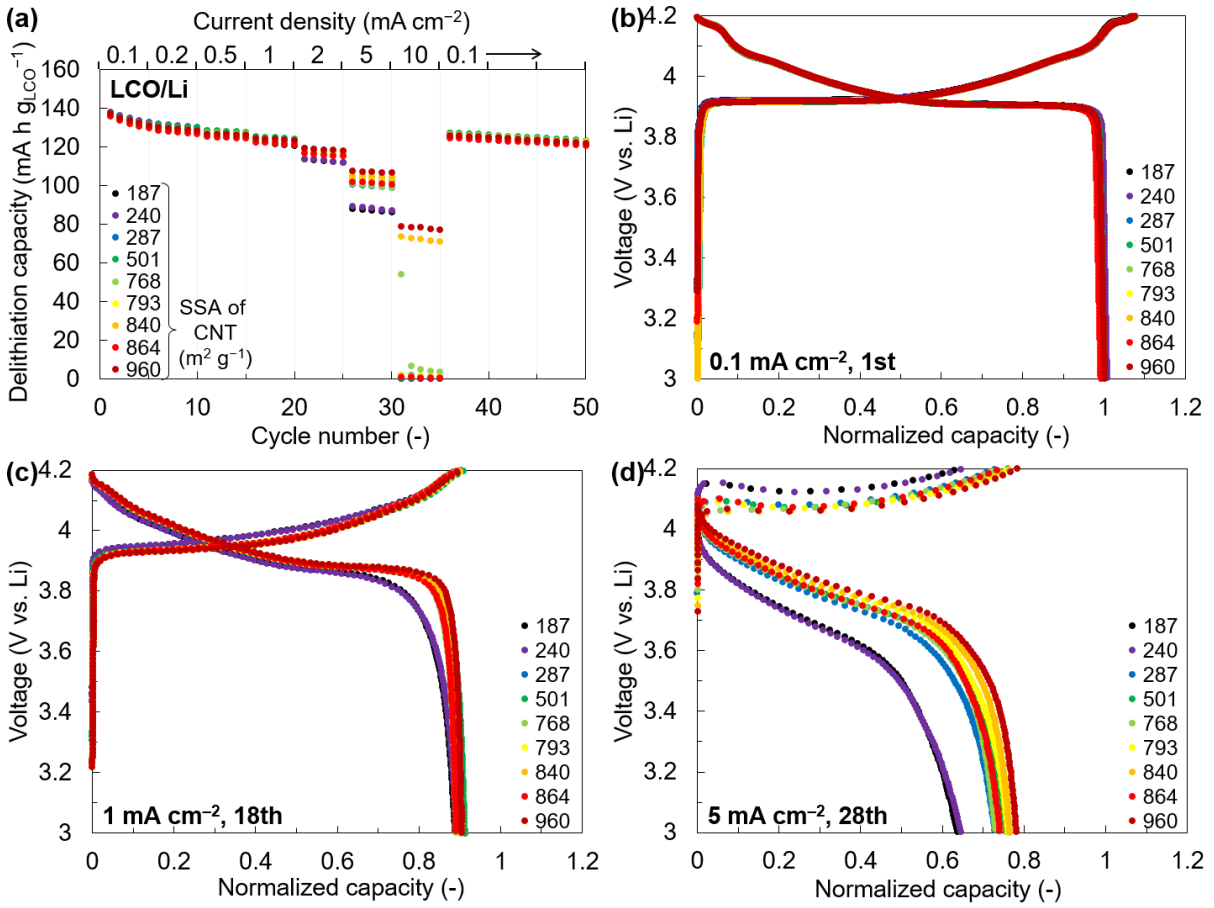

Fig. 2.3. Cycle and rate performance of LCO/Li half cells made of electrodes based on CNTs with various SSAs. (a) Cycle performance with current densities changed for different cycles. (b–d) Delithiation-lithiation curves with capacity normalized to the calculated capacity of LCO (product of areal mass and theoretical capacity for LCO).

Fig. 2.4 shows the cycle and rate performance of the graphite/Li half cells. The half cells showed a delithiation capacity close to the theoretical capacity for graphite (372 mA h g_{gr}^{-1}) at a low current density of 0.1 mA cm^{-2}, which stayed high for 0.2–0.5 mA cm^{-2}, then decreased significantly for 1–10 mA cm^{-2}. The capacities were slightly higher for the CNTs with larger SSAs (840–960 m^2 g^{-1}) at low current densities (0.1–0.5 mA cm^{-2}) but were different at high current densities (1–10 mA cm^{-2}). After returning to the current density of 0.1 mA cm^{-2}, the capacity returned to 350–370 mA h g_{gr}^{-1} and stayed stable during cycling (Fig. 2.4a). The lithiation-delithiation curves at 0.1 mA cm^{-2} and the 1st cycle (Fig. 2.4b) showed a huge capacity at 0.2–0.9 V vs. Li because of reductive decomposition

of the electrolyte [22]. As a result, a solid electrolyte interphase (SEI) formed on the negative electrode, which prevented further decomposition of the electrolyte, causing a small irreversible capacity in later cycles. The capacity for SEI formation corresponds to 10%–40% of the theoretical capacity for graphite, and is greater for the CNTs with larger SSAs, resulting in greater initial irreversible capacities (the difference between the lithiation and delithiation capacities). The three plateaus corresponding to the different stage structures were evident, showing sufficient electrical conduction in the graphite-CNT at the low current density of 0.1 mA cm^{-2}. At the moderate current density of 1 mA cm^{-2}, the plateau decreased and reached the cut-off voltage of 0 V vs. Li at 50%–70% of the theoretical capacity for graphite in the lithiation (Fig. 2.4c). The incomplete lithiation resulted in smaller delithiation capacities. There was no clear correlation between the lithiation/delithiation capacities and the SSAs, possibly because the slight difference in overpotential resulted in a huge difference in lithiation, owing to the narrow voltage window for lithiation (0–0.2 V vs. Li). At the high current density of 5 mA cm^{-2}, all the graphite-CNT electrodes showed small capacities (< 15% of the theoretical capacity for graphite) because of the narrow voltage window for lithiation (Fig. 2.4d). In the graphite-CNT electrode, the irreversible capacity was smaller for CNTs with smaller SSAs, but no clear correlation was found between the rate performance and SSAs, possibly owing to the enhanced electrical conductivity of graphite compared with LCO.

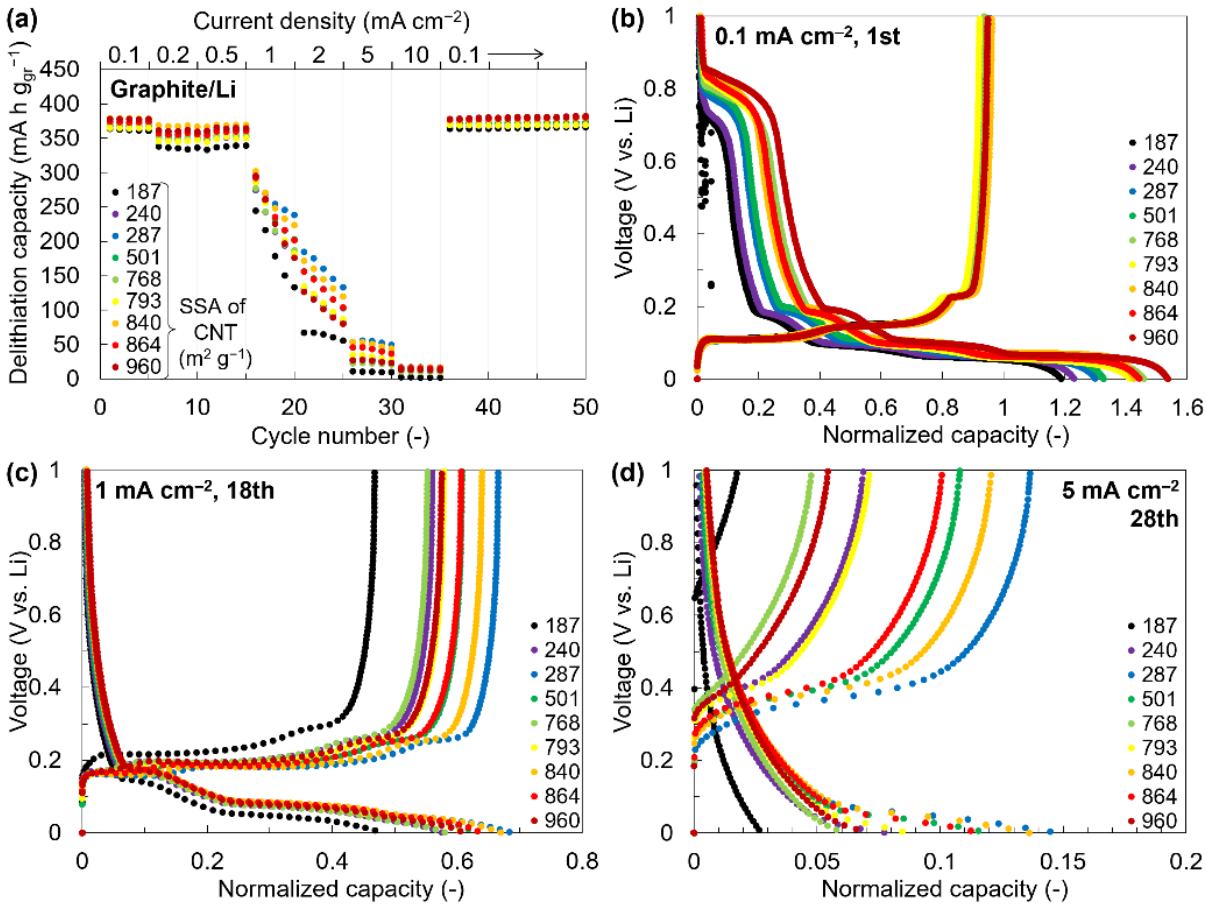

Fig. 2.4. Cycle and rate performance of graphite/Li half cells made of electrodes based on CNTs with various SSAs. (a) Cycle performance with current densities changed for different cycles. (b–d) Lithiation-delithiation curves with capacity normalized to the calculated capacity of graphite (product of areal mass and theoretical capacity for graphite).

Fig. 2.5 shows the cycle and rate performance of the graphite/LCO full cells. In contrast with the half cells (Figs. 2.3a and 2.4a), the initial discharge capacities were smaller than the theoretical ones and changed depending on the SSA of the CNTs, from 123 and 121 mA h g_{LCO}^{-1} for the SSAs of 187 and 240 m^2 g^{-1}, respectively, to 92 mA h g_{LCO}^{-1} for the SSAs of both 864 and 960 m^2 g^{-1}. The discharge capacity decreased with increasing current density from 0.1 to 10 mA cm^{-2}. Fig. 2.5b shows the charge-discharge curves at the 1st cycle. In the first charge, the cells showed a normalized charge capacity of 0.2–0.4 at 3.1–3.7 V, which corresponds to the SEI formation on the graphite-CNT electrode found in Fig. 2.4b. Then, the normalized charge capacity increased linearly at 3.7–4.2 V,

reaching ~1.2 at the cut-off voltage of 4.2 V. The initial charge capacity was 20% larger than the theoretical one because of the capacity related to the SEI formation. In the first discharge, the voltage decreased almost linearly from 4.2 to 3.7 V, then quickly decreased to the cut-off voltage of 3.0 V. The normalized discharge capacity was large (~0.9) for the CNTs with small SSAs (187 and 240 m^2 g^{-1}) and small (≤ 0.7) for the CNTs with large SSAs (840–960 m^2 g^{-1}). At the moderate current density of 1 mA cm^{-2} at the 18th cycle (Fig. 2.5c), the charge curve showed small capacity over the voltage range of 3.0–3.7 V because of the completed SEI formation in the initial cycles and showed a linear voltage increase from 3.8 V, 0.1 V higher than the charge curve at 0.1 mA cm^{-2}. The discharge curve showed a linear voltage decrease from 4.1 to 3.6 V, 0.1 V lower than the discharge curve at 0.1 mA cm^{-2}. The shift of 0.1 V for the voltage range indicates the increased charge/discharge overvoltage at 1 mA cm^{-2} compared to the case at 0.1 mA cm^{-2}. The normalized discharge capacity was ~0.8 for the CNTs with SSAs of 187 and 240 m^2 g^{-1} and ~0.55 for the CNTs with SSAs of 840–860 m^2 g^{-1}. The smaller discharge capacities for the CNTs with larger SSAs are due to the larger irreversible capacity at the first cycle (Fig. 2.5b). At the high current density of 5 mA cm^{-2} (Fig. 2.5d), the charge curves showed an almost linear increase from 3.9 to 4.2 V, and the discharge curves showed an almost linear decrease from 4.0 to 3.5 V. The overvoltage for charge and discharge increased by 0.1 V compared to that at 1 mA cm^{-2}. Differently from the graphite/Li half cell, where the lithiation of graphite easily reached the cut-off voltage of 0 V vs. Li, lithiation of graphite (charge of the cell) occurred over a wider voltage range of 3.9–4.2 V, resulting in retained normalized discharge capacities between 0.37 (with CNT SSA of 960 m^2 g^{-1}) and 0.61 (with CNT SSA of 287 m^2 g^{-1}). The discharge capacity was largest for the CNT SSA of 287 m^2 g^{-1} because of the improved rate performance compared with the CNT SSAs of 187 and 240 m^2 g^{-1}. The CNT SSA of 287 m^2 g^{-1} may have provided sufficient electrical conduction pathways for the LCO particles in the LCO-CNT positive electrode, in addition to the small irreversible capacity for the SEI formation on the graphite-CNT negative electrode.

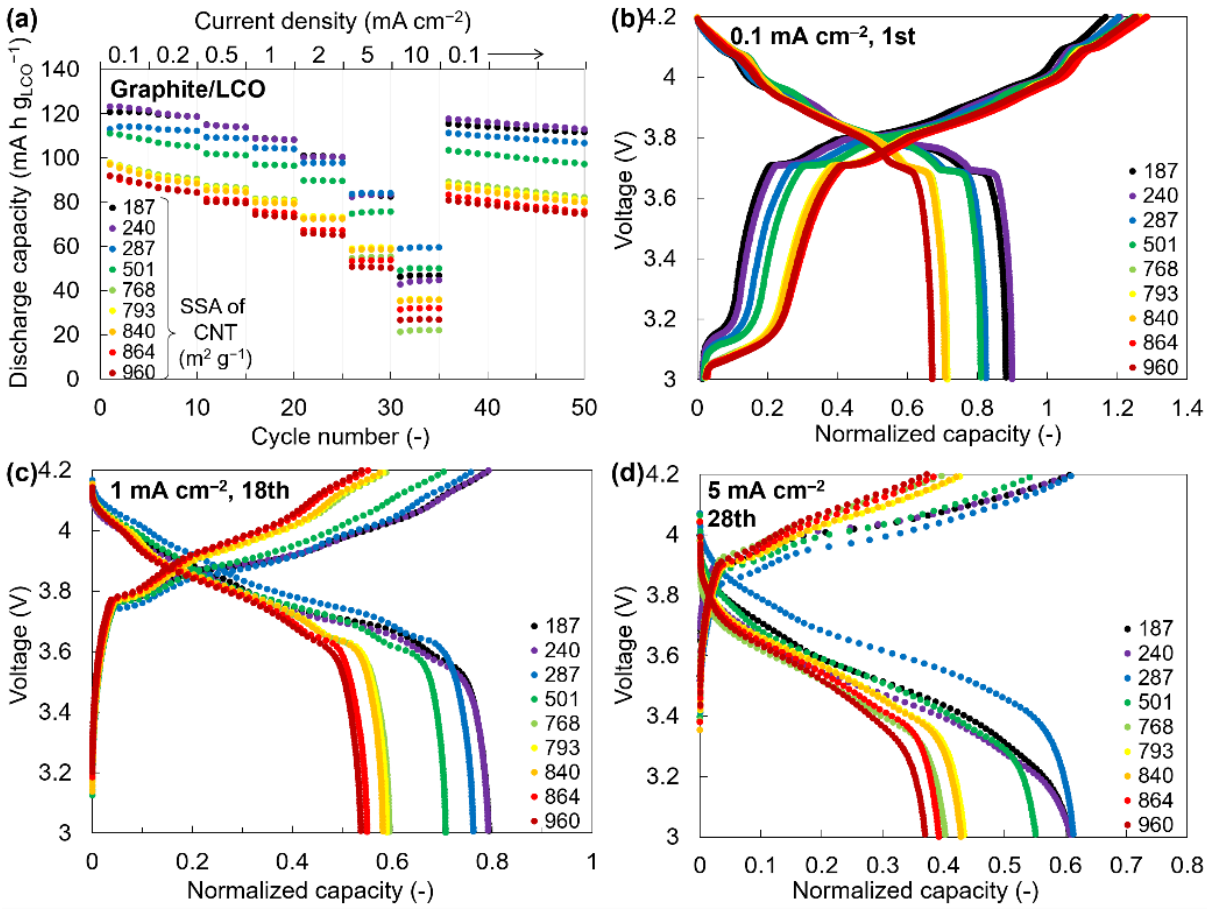

Fig. 2.5. Cycle and rate performance of graphite/LCO full cells made of electrodes based on CNTs with various SSAs. (a) Cycle performance with current densities changed for different cycles. (b–d) Charge-discharge curves with capacity normalized to the calculated capacity of LCO (product of areal mass and theoretical capacity for LCO).

The irreversible capacities, reversible capacities, and Coulombic efficiencies at the first cycle are summarized in Fig. 2.6. The LCO/Li cells showed a normalized irreversible capacity of < 0.1, which only changed slightly with the SSAs of the CNTs, whereas the graphite/Li and graphite/LCO cells showed much larger values of 0.2–0.6, which were proportional to the SSAs of the CNTs (Fig. 2.6a). The fitting curve for the graphite/Li half cell showed a y-intercept of 0.174 and a slope of 3.50×10^{-4}. Graphite particles with an SSA of 9.4 $m^2\ g_{gr}^{-1}$ provide an SSA of 9.1 $m^2\ g_{electrode}^{-1}$ at a concentration of 97 mass%, whereas CNTs with SSAs of 187–960 $m^2\ g_{CNT}^{-1}$ provide SSAs of 5.6–29 $m^2\ g_{electrode}^{-1}$ at a concentration of 3 mass%. The y-intercept indicates the irreversible capacity corresponding to

the graphite particles contained at 97 mass%, which is normalized with the theoretical capacity for graphite (372 mA h g_{gr}^{-1}). Thus, the irreversible capacity per graphite surface area is calculated as $0.174\times(372\times0.97)/(9.4\times0.97) = 6.9$ mA h m^{-2}_{gr}. The slope reveals the irreversible capacity associated with the CNT contained at 3 mass%, and the irreversible capacity per CNT surface area is calculated as $3.50\times10^{-4}\times(372\times0.97)/0.03 = 4.2$ mA h m^{-2}_{CNT}. The values are similar but different, which is likely because of the differences between the surface structures of graphite (basal plane and edge plane) and CNTs (curved basal plane). The difference in the irreversible capacity between the graphite/Li and graphite/LCO cells is similar to the irreversible capacity for the LCO/Li cell, therefore the irreversible capacities related to the graphite-CNT and LCO-CNT electrodes should be mostly responsible for the irreversible capacity of the graphite/LCO full cell.

The normalized reversible capacities (Fig. 2.6b) were close to 1 for the graphite/Li and LCO/Li half cells despite their non-negligible irreversible capacities. However, the reversible capacity was smaller than 1 and decreased significantly from ~0.9 to ~0.7 with increasing SSA of the CNTs for the graphite/LCO full cell. The half cells contained excess Li in the Li counter electrode (~100 mA h cm^{-2} for 500 μm-thick Li foil), whereas the full cell did not contain excess Li at 1 mA h cm^{-2}. This result shows that the CNT-based electrodes do not lose their capacity because of the irreversible capacity when additional Li is supplied (half cells), whereas the full cell loses its capacity because it loses active Li in the irreversible reaction. Fig. 2.6c highlights the effect of the CNT SSA on the irreversible and reversible capacities of the full cell. The initial Coulombic efficiency was high for the LCO/Li half cell because of the small irreversible capacity, moderate for the graphite/Li half cell because of the irreversible capacity related to the SEI formation on the graphite-CNT electrode, and low for the graphite/LCO full cell because of the irreversible capacity and consumption of active Li related to the SEI formation on the graphite-CNT electrode (Fig. 2.6d). It is necessary to use CNTs with relatively small SSA (around 200–300 m^2 g^{-1}) for low irreversible capacity and high Coulombic efficiency.

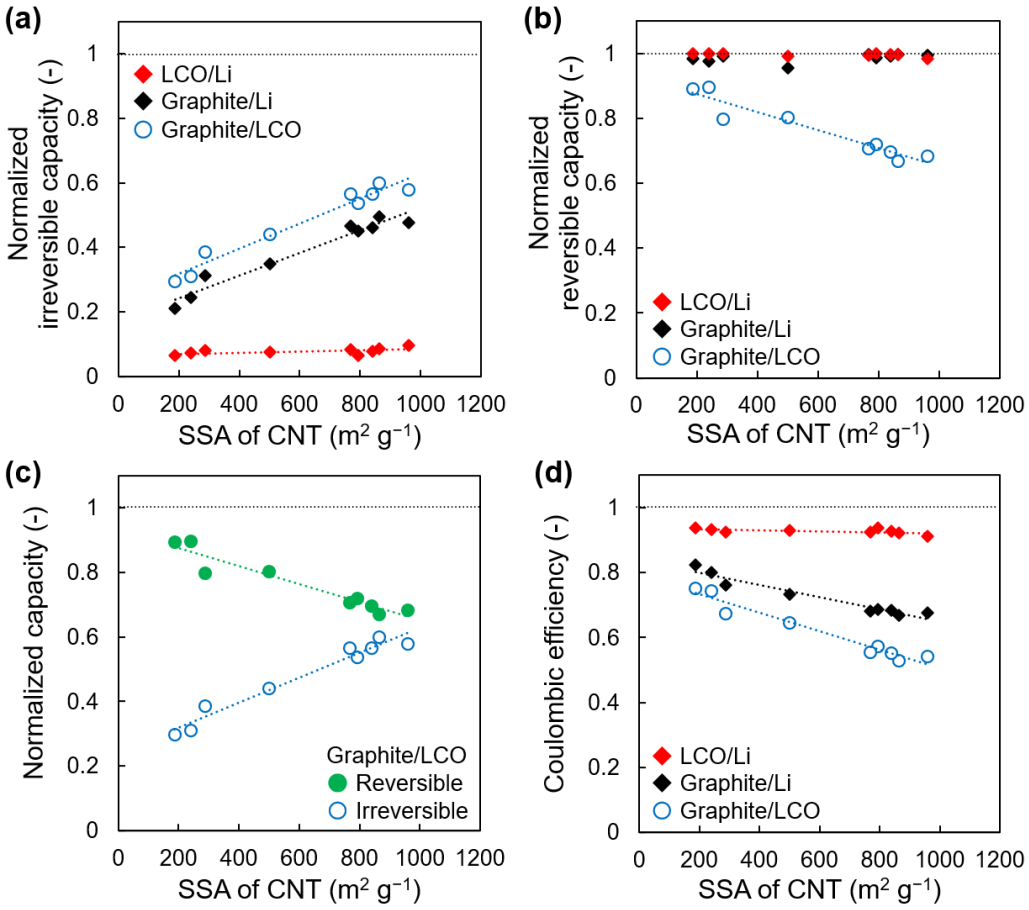

Fig. 2.6. Normalized irreversible capacities, reversible capacities, and Coulombic efficiencies at the first cycle and 0.1 mA cm^{-2}. (a) Normalized irreversible capacities. (b) Normalized reversible capacities. (c) Reversible and irreversible capacities of graphite/LCO full cell. (d) Coulombic efficiencies.

2.3.3 Cycle performance of the graphite/LCO full cell

Next, the cycle performance of the graphite/LCO full cell was evaluated for 300 cycles. The discharge capacity was greater for the cell made of CNTs with smaller SSAs (187 and 240 m^2 g^{-1}) and gradually decreased during cycling for all the cells, regardless of the CNT SSA (Fig. 2.7a). Coulombic efficiency increased quickly in the early cycles, exceeding 0.98 at the 10th cycle for any CNT SSA (Fig. 2.7b). Coulombic efficiency was greater for the cell made using CNTs with smaller SSA (187 m^2 g^{-1}) than that for cell made using CNTs with larger SSA (960 m^2 g^{-1}), showing that slow side reactions continuously occurred for later cycles on the surface of CNTs. Charge-discharge

curves are shown for the cell made using CNTs with a moderate SSA of 501 m^2 g^{-1} (Fig. 2.7c). The charge curve upshifted while the discharge curve downshifted by 0.05–0.1 V from the 1st to the 50th cycle, gradually increasing the overvoltage with increasing cycles. Thus, the CNTs should not have too large of an SSA, to achieve high Coulombic efficiency and low overvoltage.

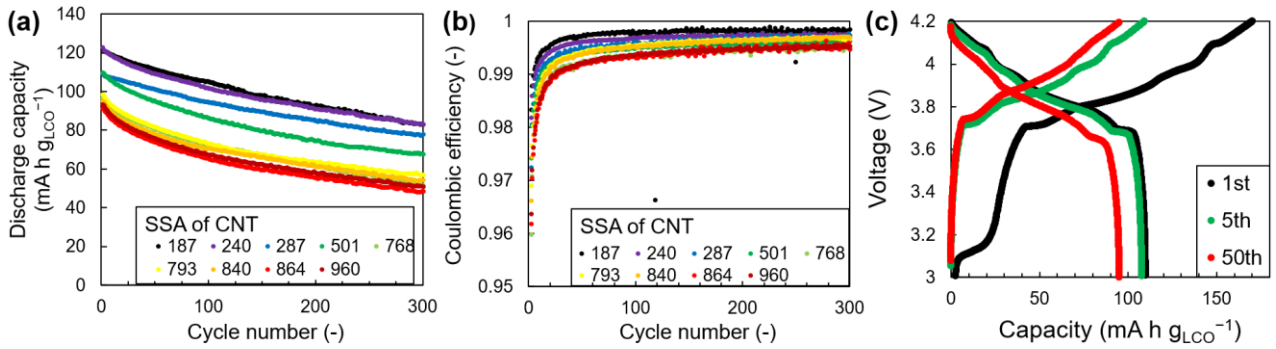

Fig. 2.7 Cycle performance of the graphite/LCO full cell. (a) Discharge capacity. (b) Coulombic efficiency. (c) Charge-discharge curves for the full cell made using the CNT with SSA of 501 m^2 g^{-1} (type E). The 1st cycle was performed at 0.1 mA cm^{-2} and later cycles were performed at 0.3 mA cm^{-2}.

Coulombic efficiency was evaluated for the graphite/LCO full cells made with CNT of various SSAs at the 1st, 5th, and 50th cycle (Fig. 2.8). Coulombic efficiency was low (between 0.5 and 0.8) at the 1st cycle but improved significantly to > 0.97 and > 0.99 at the 5th and 50th cycle, respectively (Fig. 2.8a). Coulombic efficiencies shown for a narrow range (Fig. 2.8b) reveal that the Coulombic efficiency decreased linearly with increasing SSA at the 5th and 50th cycles. Even after the SEI formation at the 1st cycle, CNTs continuously cause slow side reactions, such as reductive decomposition of the electrolyte, and thus, CNTs should not have too large of an SSA, to achieve high Coulombic efficiency.

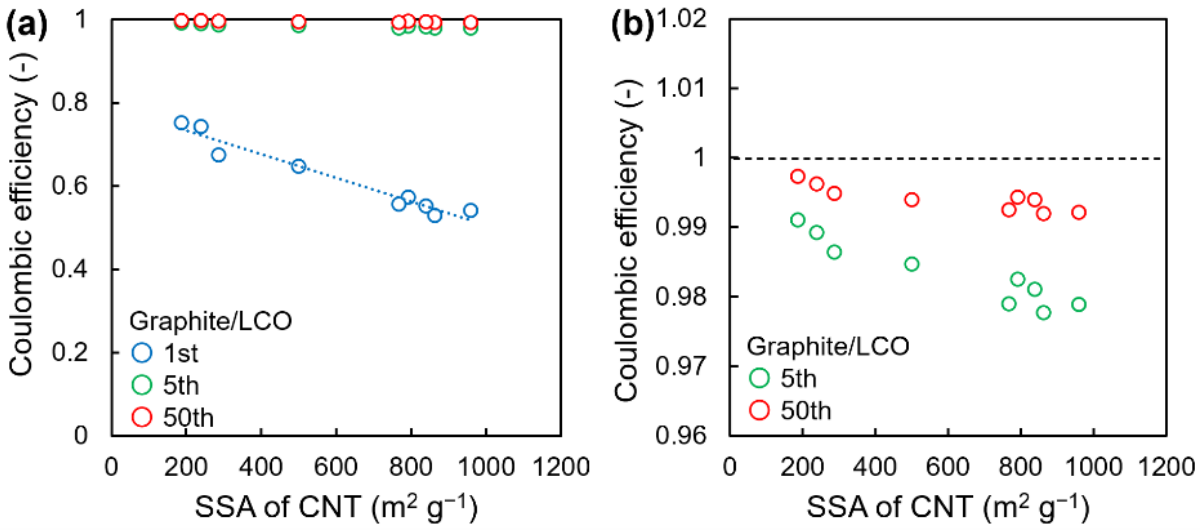

Fig. 2.8. Effect of CNT SSA on Coulombic efficiency of the graphite/LCO full cell, shown for (a) a full range and (b) a narrow range.

In summary, CNTs with large SSAs can provide more electrical conduction pathways for the LCO particles, but an excessively large surface area causes surplus irreversible capacity because of the SEI formation on the graphite-CNT negative electrode and decreased reversible capacity of the graphite-CNT/LCO-CNT full cell. In contrast, CNTs with small SSA achieve high reversible capacity with suppressed irreversible capacity. Notably, CNTs with small SSA may have disadvantages in rate performance, if the electrical conductivity of active materials is not sufficiently high. From these results, CNTs with an SSA of ~300 m^2 g^{-1} and lengths greater than several tens of micrometers are suitable for the 3D sponge-like current collector, achieving a high reversible capacity and rate performance.

2.4 Conclusion

CNTs with various lengths (56–226 μm), average diameters (5–14 nm), and SSAs (187–960 m^2 g^{-1}) were systematically studied as 3D current collectors for LIBs. All CNTs, except for one type, were suitable for fabricating self-supporting electrodes of graphite-CNT and LCO-CNT with a CNT content as low as 3 mass%, prepared using a simple co-dispersion and co-filtration process. Within

these ranges, a large CNT length and SSA are suitable for making self-supporting electrodes without metal foils or polymeric binders and provide sufficient electrical conduction paths to the active materials with poor electrical conductivities such as LCO. However, a large SSA causes excess electrolyte decomposition in the negative electrode, resulting in an irreversible loss of capacity and depletion of active Li ions. Therefore, CNTs with smaller SSAs of 187–240 m^2 g^{-1} are more beneficial for high reversible capacity at low charge-discharge rates, while those with relatively small SSA of ~300 m^2 g^{-1} are favorable for achieving a higher rate performance. A CNT-based electrode architecture with an optimal CNT structure will enable lightweight rechargeable batteries with high energy density.

Acknowledgments

The authors thank Zeon Corporation for some of the CNT powder samples. This work is financially supported by Grand-in-Aid for Scientific Research (S) and (A) from the Japan Society for the Promotion of Science (Grant numbers: JP16H06368 and JP21H04633) and by Zeon Corporation.

Supplementary

Properties for self-supporting paper. The CNTs with larger SSA have thinner walls (SWCNTs have a SSA of 1315 m^2 g^{-1} theoretically), tend to be thinner, flexible and bendable. It is known that the van der Waals force makes the interaction between CNTs strong, which facilitates the formation of a self-supporting paper [23,24]. Another point is that the closer the CNTs are to the single wall, the more total length per CNT mass can be gained, which facilitates the development of a network structure. It is known that when SSA is small, the properties of CNTs are similar to those of carbon fiber, and since it is thick and rigid, the materials tend to have point contact with each other and do not form a self-supporting paper even if more than 10 mass% is added because the interactions are weak [8]. Regarding length, it is known from a study on CNT papers that the longer the CNT length, the higher the strength and electrical conductivity [25], and this would be also true in the case of the composite

films with small CNT content in this research in this research.

References

[1] V. Etacheri, R. Marom, R. Elazari, G. Salitra, D. Aurbach, Challenges in the development of advanced Li-ion batteries: a review, Energy Environ. Sci. 4 (2011) 3243–3262.

[2] Y. Ding, Z. P. Cano, A. Yu, J. Lu, Z. Chen, Automotive Li ion batteries: Current status and future perspectives, Electrochem. Energy Rev. 2 (2019) 1–28.

[3] L. Pierucci, The quality of experience perspective toward 5G technology, IEEE Wireless Commun. 22 (2015) 10–16.

[4] B. Dong, Q. Shi, Y. Yang, F. Wen, Z. Zhang, C. Lee, Technology evolution from self-powered sensors to AIoT enabled smart homes, Nano Energy 79 (2021) 105414–105436.

[5] M. Hagen, D. Hanselmann, K. Ahlbrecht, R. Maça, D. Gerber, J. Tübke, Lithium–sulfur cells: The gap between the state-of-the-art and the requirements for high energy battery cells, Adv. Energy Mater. 5 (2015) 1401986–1401996.

[6] S. W. Lee, B. M. Gallant, Y. Lee, N. Yoshida, D. Y. Kim, Y. Yamada, et al., Self-standing positive electrodes of oxidized few-walled carbon nanotubes for light-weight and high-power lithium batteries, Energy Environ. Sci. 5 (2012) 5437–5444.

[7] R. Quintero, D. Y. Kim, K. Hasegawa, Y. Yamada, A. Yamada, S. Noda, Carbon nanotube 3D current collectors for lightweight, high performance and low cost supercapacitor electrodes, RSC Adv. 4 (2014) 8230–8237.

[8] K. Hasegawa, S. Noda, Lithium ion batteries made of electrodes with 99 wt% active materials and 1 wt% carbon nanotubes without binder or metal foils, J. Power Sources 321 (2016) 155–162.

[9] B. H. Nguyen, V. H. Nguyen, Promising applications of graphene and graphene-based nanostructures, Adv. Nat. Sci.: Nanosci. Nanotechnol. 7 (2016) 023002–023016.

[10] H.-C. Tao, L.-Z. Fan, Y. Mei, X. Qu, Self-supporting Si/reduced graphene oxide nanocomposite films as anode for lithium ion batteries, Electrochem. Commun. 13 (2011) 1332–1335.

[11] X. Zhang, Y. Li, Y. Lin, T. Yang, M. Shi, W. Xu, A flexible LiFePO4/carbon nanotube/reduced graphene oxide film as self-supporting cathode electrode for lithium-ion battery, Ionics 26 (2020) 1537–1546.

[12] K. Kaneko, K. Hori, S. Noda, Nanotubes make battery lighter and safer, Carbon 167 (2020) 596–600.

[13] T. Kowase, K. Hori, K. Hasegawa, T. Momma, S. Noda, A-few-second synthesis of silicon

nanoparticles by gas-evaporation and their self-supporting electrodes based on carbon nanotube matrix for lithium secondary battery anodes, J. Power Sources 363 (2017) 450–459.

[14] L. Cui, L. Hu, J. W. Choi, Y. Cui, Light-weight free-standing carbon nanotube-silicon films for anodes of lithium ion batteries, ACS Nano 4 (2010) 3671–3678.

[15] K. Hori, Y. Yamada, T. Momma, S. Noda, High-energy density LixSi-S full cell based on 3D current collector of few-wall carbon nanotube sponge, Carbon 161 (2020) 612–621.

[16] K. Hori, K. Hasegawa, T. Momma, S. Noda, Volumetric discharge capacity 1 A h cm–3 realized by sulfur in carbon nanotube sponge cathodes, J. Phys. Chem. C 123 (2019) 3951–3958.

[17] Y. Yoshie, K. Hori, T. Mae, S. Noda, High-energy-density Li–S battery with positive electrode of lithium polysulfides held by carbon nanotube sponge, Carbon 182 (2021) 32–41.

[18] G. Yang, J. Tan, H. Jin, Y. H. Kim, X. Yang, D. H. Son, et al., Creating effective nanoreactors on carbon nanotubes with mechanochemical treatments for high-areal-capacity sulfur cathodes and lithium anodes, Adv. Funct. Mater. 28 (2018) 1800595–1800603.

[19] D. Y. Kim, H. Sugime, K. Hasegawa, T. Osawa, S. Noda, Fluidized-bed synthesis of sub-millimeter-long single walled carbon nanotube arrays, Carbon 50 (2012) 1538–1545.

[20] Z. Chen, D. Y. Kim, K. Hasegawa, T. Osawa, S. Noda, Over 99.6 wt%-pure, sub-millimeter-long carbon nanotubes realized by fluidized-bed with careful control of the catalyst and carbon feeds, Carbon 80 (2014) 339–350.

[21] M. Li, M. Risa, T. Osawa, H. Sugime, S. Noda, Facile catalyst deposition using mists for fluidized-bed production of sub-millimeter-long carbon nanotubes, Carbon 167 (2020) 256–263.

[22] S. J. An, J. Li, C. Daniel, D. Mohanty, S. Nagpure, D. L. Wood, The state of understanding of the lithium-ion-battery graphite solid electrolyte interphase (SEI) and its relationship to formation cycling, Carbon 105 (2016) 52–76.

[23] S. C. Her, W. C. Hsu, Strain and Temperature Sensitivities Along with Mechanical Properties of CNT Buckypaper Sensors, Sensors 20 (2020) 3067–3079.

[24] J. Y. Oh, S. J. Yang, J. Y. Park, T. Kim, K. Lee, Y. S. Kim, H. N. Han, C. R. Park, Easy Preparation of Self-Assembled High-Density Buckypaper with Enhanced Mechanical Properties Nano Lett. 15 (2015) 190−197.

[25] S. Sakurai, F. Kamada, D. N Futaba, M. Yumura, K. Hata, Influence of lengths of millimeter-scale single-walled carbon nanotube on electrical and mechanical properties of buckypaper, Nanoscale Research Letters 8 (2013) 546−552.

Chapter 3. Battery architecture consist of CNT and BNNT

The content of this Chapter has been published in: K. Kaneko, K. Hori, and S. Noda*, "Nanotubes make battery lighter and safer," Carbon 167, 596-600 (2020). DOI: 10.1016/j.carbon.2020.06.042

3.1 Objective

Batteries with a high energy density are in great demand toward their more active utilizations and versatile applications. The energy density of batteries is increasing year by year [1], but the risk of accidents increases with energy density [2]. To achieve safer batteries with a higher energy density, the selection of the separator becomes crucially important since it prevents the direct contact and runaway reaction between the negative and positive electrodes. The separators used for the conventional lithium-ion batteries (LIBs) are made of polyolefins that ensure safety by a shutdown function which prevents the thermal runaway by closing the pores and stopping further reaction when the temperature of the batteries increases abnormally. However, its thermal stability is intrinsically low because of the low melting points of 130 °C (polyethylene, PE) and 165 °C (polypropylene, PP) [3]. To improve thermal stability, many types of separator have been reported [4]; (i) ceramic coating or ceramic-polymer composite (e.g. SiO_2, Al_2O_3) [5], (ii) multi-layered structure (e.g. PP/PE or more layers) [3,6], (iii) replacement of polyolefins with highly heat-resistant polymers (e.g. polyethylene terephthalate, polytetrafluoroethylene) [7]. These approaches are effective to some extent, but the thermal stability is not very high due to the intrinsic thermal property of organic compounds. Polymer-based separators shrink or decompose when heated excessively (~200 °C), resulting in the direct contact between the negative and positive electrodes and battery runaway [3]. Therefore, a totally new approach without using organic compounds is required for the realization of highly stable separators that do not shrink and get damaged at high temperature.

We propose to use inorganic nanotubes that show binding nature and yield self-supporting sponge-like films. Electrically conductive carbon nanotube (CNT) has been used as 3D current collector for various active materials, in which CNT played the roles as the binder, conductive filler,

and current collector [8,9]. Graphene, especially reduced graphene oxide (rGO), has been extensively used for battery electrodes as conductive additives. Self-supporting electrodes have also been reported using graphene, but its content in electrode is typically as high as 20–50 wt% [10,11]. In addition, graphene is 2D material that can be used for gas barrier [12], and thus can inhibit the ionic diffusion when used for battery electrodes at large content. Contrarily, CNT can yield self-supporting electrode by adding a tiny amount of only 1 wt% and hold active materials at very high content of 99 wt% [8]. CNT has a 1D structure that yields interwoven network, that will be the origin for its very high self-supporting nature.

Here, we propose to use boron nitride nanotube (BNNT), which has high chemical and thermal stabilities (air-stable up to 900 °C) [13], for the separator. Fig. 3.1 compares the conventional architecture with our proposed architecture based on nanotubes. Conventional architecture uses organic polymers that are not thermally stable for the separator and the binder (Fig. 3.1a). In addition, it uses heavy foils of metals, resulting in a significant mass fraction of non-active materials (25.0%) in the electrode/separator stack (Fig. 3.1b) [14]. On the contrary, the proposed architecture based on nanotubes uses thermally stable BNNT for the separator (Fig. 3.1c) and small amounts of CNT (3 wt% of the total electrode mass) for the binder, conductive filler, and current collector. As a result, the mass fraction of non-active materials was decreased to 6.4% and that of active materials was increased to 93.6% in this work (Fig. 3.1d). In case of practical large cells, the CNT-based electrodes can be used in combination with metallic combs or wires to carry large current that weigh < 1/10 of metallic foils [8].

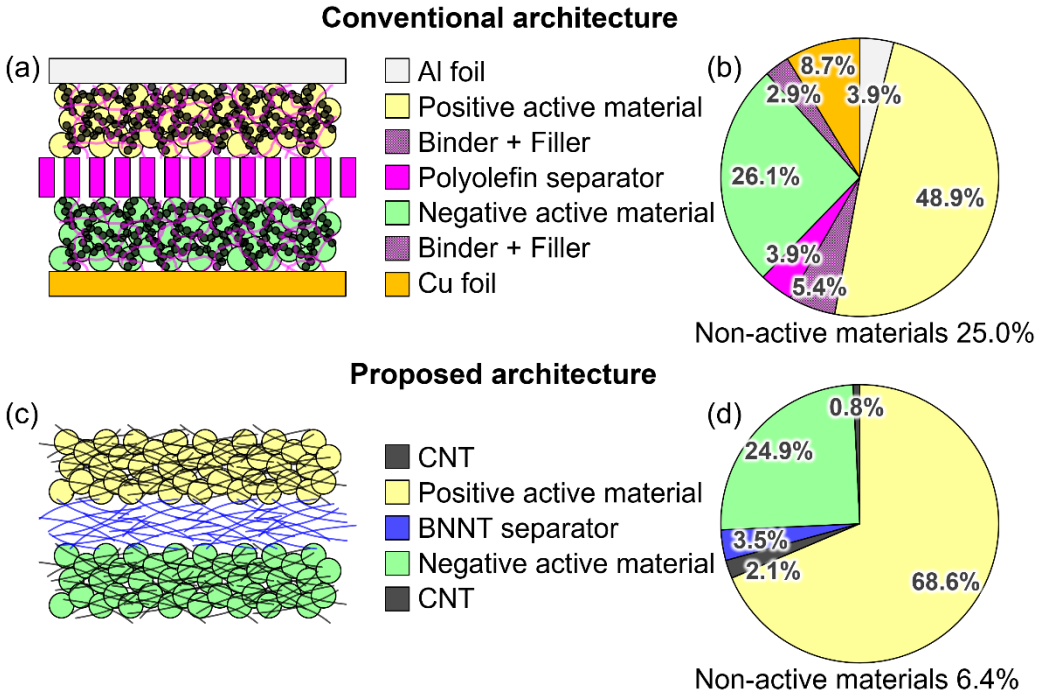

Fig. 3.1. Conventional and proposed full-cell architectures. (a) Conventional architecture that uses organic polymer for the separator and the binder, carbon black for the conductive filler, and metallic foils for the current collector. (b) Weight distribution of the materials in the electrode/separator stack calculated for the current benchmark of Panasonic NCR18650B battery based on the report by Hagen et al. [14]. (c) Proposed architecture that uses BNNT for the separator and CNT for the binder, conductive filler, and current collector. (d) Weight distribution of the materials in the cell of this work (Fig. 3.4d). Detailed data for (b) and (d) are provided in Tables S3.1 and S3.2.

3.2 Experimental

Fabrication of BNNT Separator and CNT-Based Electrodes: The self-supporting BNNT separator was fabricated by dispersion and filtration. BNNT puff ball (BNNT, LLC; length of < 200 μm, average wall number of 2–3, specific surface area of ~200 $m^2\ g^{-1}$) was dispersed in 2-propanol (FUJIFILM Wako Pure Chemical Co., Osaka, Japan) by sonication (bath-type VS-50R, VELVO-CLEAR, Japan) for 20 min at a concentration of 0.1 $mg_{BNNT}\ mL_{IPA}^{-1}$. The dispersed solution was vacuum-filtrated on a polytetrafluoroethylene membrane filter (PTFE filter, Merck Millipore, USA) to fabricate a self-supporting paper (mass density of 0.3 g cm^{-3}, areal mass of 0.7 mg cm^{-2}, and

thickness of 23–26 μm). The paper was dried at 120 °C in a vacuum oven for ≥ 2 h to remove 2-propanol. Similarly, the self-supporting CNT-based electrodes were fabricated by co-dispersing and filtrating CNT (synthesized by fluidized bed method [15]; length of 200–250 μm, average wall number of 2–3, a specific surface area of ~500 $m^2\ g^{-1}$) with graphite (natural graphite, SEC Carbon, Japan) or LCO (TOSHIMA Manufacturing, Japan) in 2-propanol following our previous report [8]. The diameter of the negative and positive electrodes was 7–8 and the separator was 12 mm. 0.63–0.66 mg of graphite and 1.8–1.9 mg of LCO were used for the full cell with an areal capacity of 0.6 mA h cm^{-2}, and 2.7 mg of graphite and 7.3 mg of LCO for the cell with 2.0 mA h cm^{-2}. The porosity of each separator was calculated by using the true densities of 1.4 g cm^{-3} and 0.90–0.91 g cm^{-3} for BNNT and PP, respectively [16,17].

Thermal Stability Test: The negative electrode/separator/positive electrode stack was prepared, sandwiched with SUS plates, and heated in a quartz glass tube under a N_2 atmosphere at 500 °C for 10 min. After cooling down, the electrical resistivity was checked between the two SUS plates across the stack using a digital multimeter (SANWA ELECTRIC INSTRUMENT CO., LTD., CD770, Japan). The microstructure of the separator and electrodes were evaluated using a SEM (HITACHI, S-4800, Japan) before and after heating. The thermal stability of the BNNT separator was also examined by TG-DTA (TG8120, Rigaku, Akishima, Japan) in a N_2 atmosphere at a heating rate of 10 °C min^{-1}.

Full Cell Test: 2032 type coin cells were assembled in a glove box (Unico, Ibaraki, Japan) under an Ar atmosphere (H_2O and O_2 below 1 ppmv). Coin cells were assembled with 1 M $LiPF_6$ electrolyte (Kishida Chemical, Japan) in ethylene carbonate and diethyl carbonate (v/v = 1/1) (EC:DEC; Kishida Chemical, Japan). The galvanostatic charge-discharge was conducted by a charge/discharge system (Hokuto Denko Corp., Japan). The voltage range was 3.0–4.2 V, and the charge/discharge rate was changed between 0.1C and 10C (1C = 372 mA $g^{-1}_{graphite}$) for an evaluation of rate performance.

3.3 Results and discussions

The BNNT separator was fabricated by a simple dispersion-filtration method (Fig. 3.2a). Here, just the ultrasonication was conducted for ~20 min in the dispersion process. This process can be improved with degassing and pre-stirring, then the ultrasonication is completed in ~10 min (Fig. S3.1).

The resulting BNNT separator was mechanically flexible, self-supporting (Fig. 3.2b), and exhibited high thermal stability of mass change within ±2 wt% in the thermogravimetry-differential thermal analysis (TG-DTA) (Fig. 3.2c). The BNNT separator was lighter (0.7 mg cm^{-2}, 0.3 g cm^{-3}) and more porous (~80%) than the typical PP separator (52%) at the same thickness (24 μm), thus it was expected to facilitate the Li^+ diffusion.

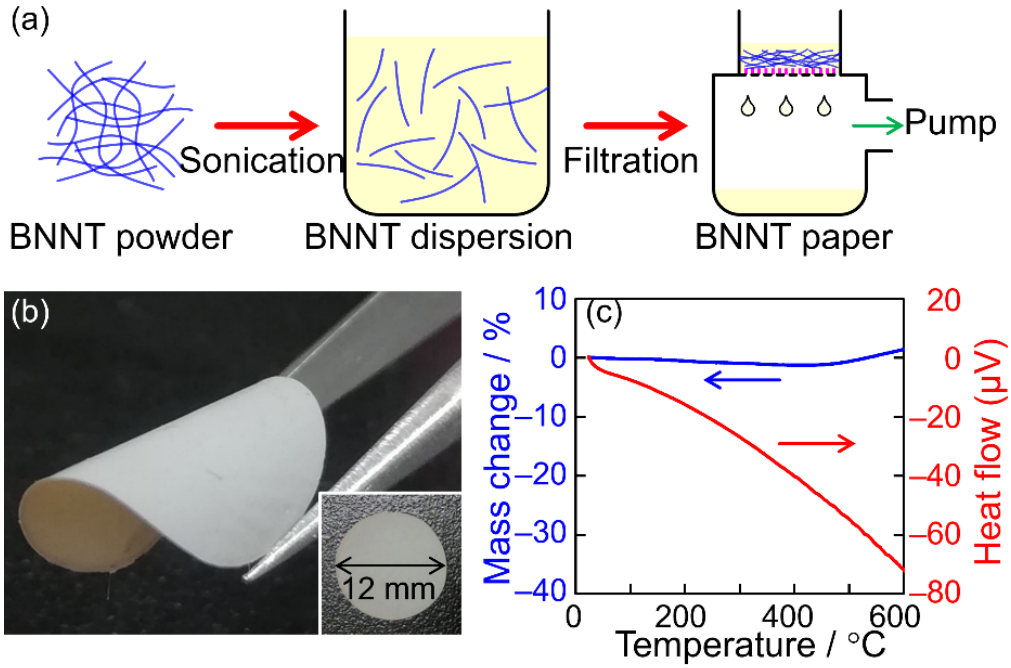

(d)

Sample	Thickness (μm)	Areal mass (mg cm^{-2})	Bulk density (g cm^{-3})	Porosity (%)
PP	24	1.06	0.44	52
BNNT	24	0.71	0.30	80

Fig. 3.2. BNNT separator of this work. (a) Fabrication procedure. (b) Photos of the BNNT separator. (c) Thermogravimetric-differential thermal analysis result of the BNNT separator under N_2 atmosphere. (d) Comparison between the conventional PP separator and the proposed BNNT separator.

The electrode/separator stacks were fabricated using the CNT-based electrodes (Fig. 3.3). The graphite-CNT negative electrode and the $LiCoO_2$ (LCO)-CNT positive electrode, which were both self-supporting in nature, were fabricated via co-dispersion and filtration [8] using submillimeter-long few-wall CNT produced by our fluidized-bed method (purity of 99 wt%, diameter of ~7 nm, length of 200–250 μm, and specific surface area of 500 $m^2\ g^{-1}$) [15]. The graphite-CNT negative electrode, PP or BNNT separator, and the LCO-CNT positive electrode were stacked, sandwiched with the stainless steel (SUS) plates, and heated under a N_2 atmosphere at 500 °C for 10 min (Fig. 3.3a). Electrode/separator stack stable at 500 °C could not be realized using organic polymers but is important for extreme environments such as Venus surface mission [18]. Glass et al. reported a primary battery made of Li-Al anode, LiCl-KCl eutectic molten salt, FeS cathode. Our architecture with CNT-based electrode and BNNT separator is compatible with such environment. We used N_2 as an inert gas to examine the thermal stability for the cases without the cell breakage. Both the PP separator (Fig. 3.3b) and the BNNT separator (Fig. 3.3c) had macropores of ~100 nm based on the scanning electron microscope (SEM) images, but the BNNT separator seemed to have a higher porosity. The nitrogen adsorption/desorption isotherm showed Type II characteristics typical for non-porous or macroporous materials [19] with SSA of = 250 $m^2\ g^{-1}$ (Fig. S3.2a). The Barrett, Joyner and Halenda (BJH-plot) (Fig. S3.2b) showed pores of two different types, A and B with volume fractions of A≪B. The pore A has a size of 1–5 nm, possibly corresponding to the inner part of individual BNNT and interspace between BNNTs in each bundle. The pore B has a wide size range of 6–200 nm, corresponding to the meso and macro pores originating from the sponge-like structure made of BNNT bundles seen in the SEM images (Fig. 3.3c and d). The pore B prevent the short-circuit between the electrodes while the porosity as high as 80% allows ions to diffuse sufficiently. The PP separator shrinks and melts at 165 °C [3], but our BNNT separator and the stack showed no changes after heating at 500 °C (Fig. 3.3d). The BNNT separator prevented the short circuit between the negative and positive electrodes.

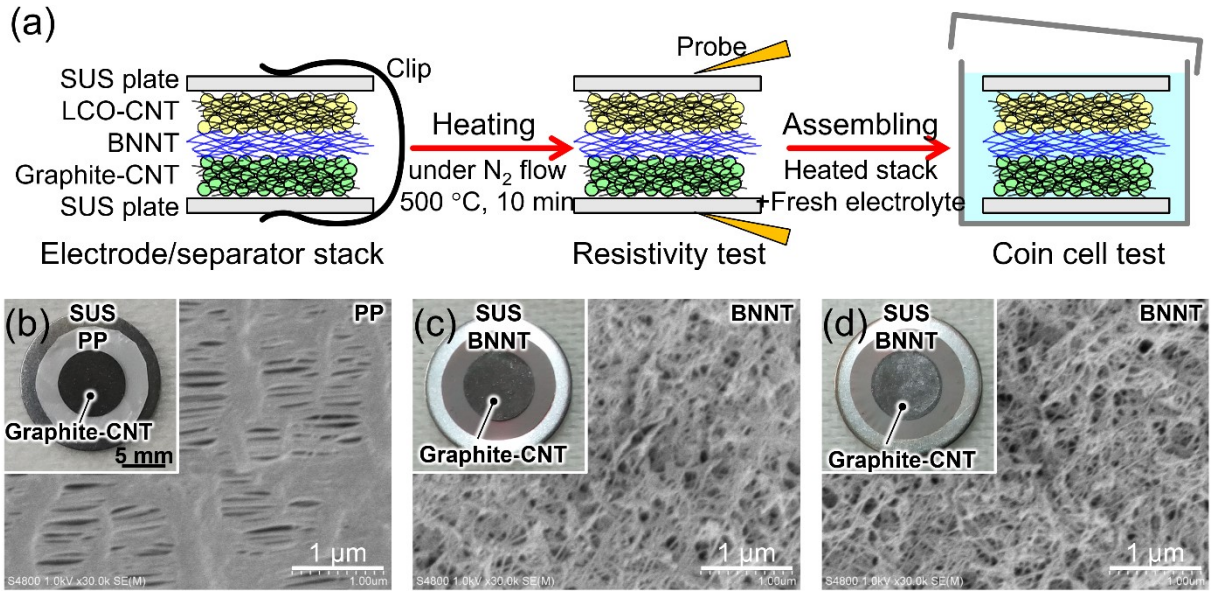

Fig. 3.3. The negative electrode/separator/positive electrode stacks and thermal stability test. (a) Procedure for the thermal stability test. (b) SEM image of the PP separator with inset photo of the as-prepared stack. (c) The BNNT separator and the as-prepared stack. (d) The BNNT separator and the stack after heating at 500 °C for 10 min.

Since no changes were observed in the graphite-CNT/BNNT/LCO-CNT stack after heating at 500 °C, a 2032 coin cell was fabricated using the heated stack and a fresh liquid electrolyte (1 M $LiPF_6$ in 1/1 v/v mixture of ethylene carbonate (EC) and diethyl carbonate (DEC)) (Fig. 3.3a). Without heating, the full cell with the BNNT separator (Fig. 3.4b) showed the same charge-discharge performances as the cell with the PP separator (Fig. 3.4a). The full cell of the heated stack with the BNNT separator showed no performance degradation, and surprisingly improved performance at a high rate possibly due to the improved junction between the CNT and active materials (Fig. 3.4c). The BNNT separator has a higher porosity (80%) than the commercial PP separator (52%) (Fig. 3.2d), that is advantageous in promoting ionic diffusion and reducing the overpotential; ~0.5 V in (c) vs ~0.7 V in (a) especially at high rates (10C). Moreover, the full cell made with the heated stack of an increased areal loading showed an excellent charge-discharge performance (Fig. 3.4d).

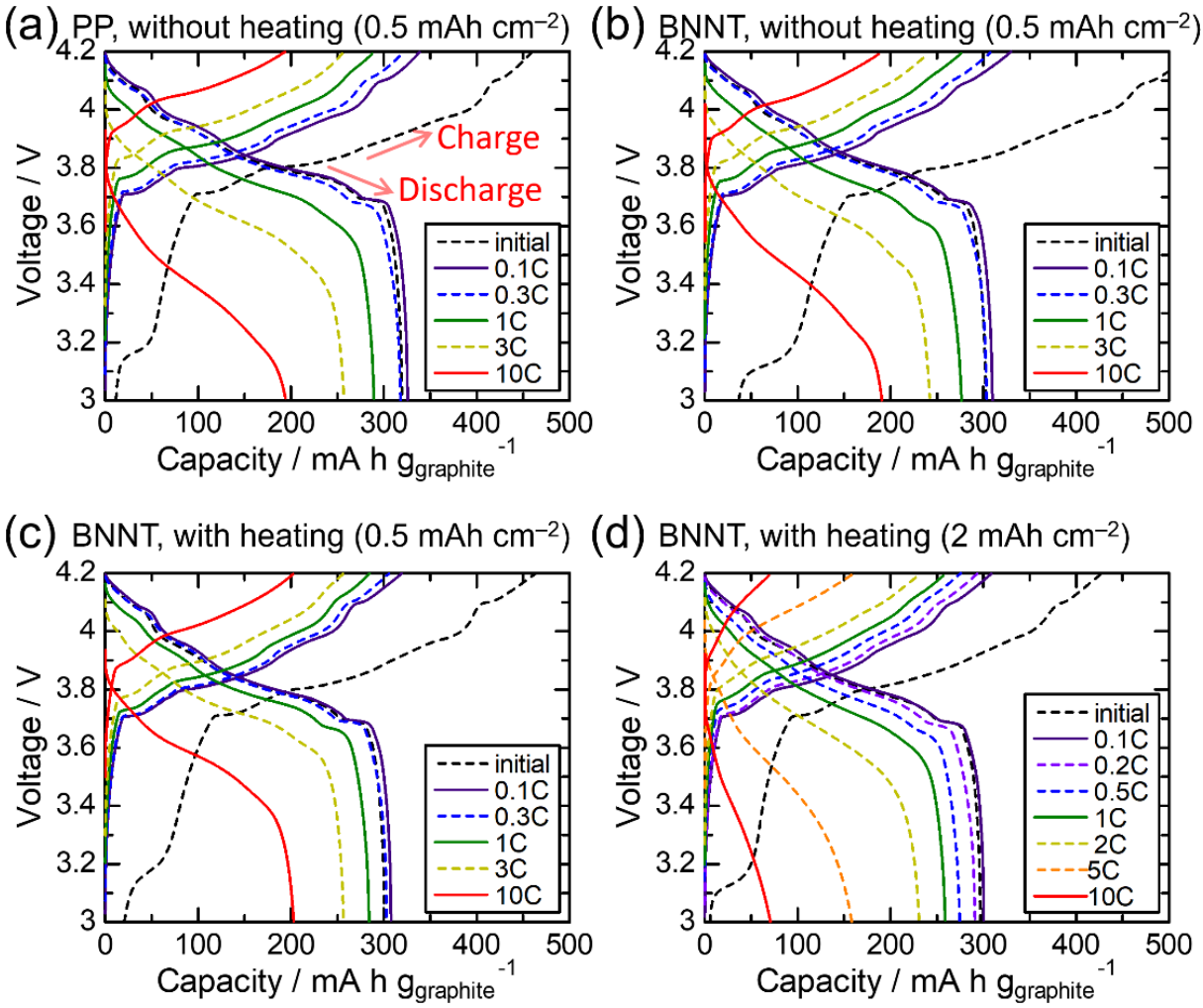

Fig. 3.4. Charge-discharge curves of the full cells made with various electrode/separator stacks. (a) The cell with a conventional PP separator without heating. (b) The cell with the BNNT separator without heating. (c,d) The cell with the BNNT separator in the electrode/separator stack heated at 500 °C. Areal loading of graphite is ~1.5 mg cm^{-2} for (a–c) and 5.3 mg cm^{-2} for (d).

Finally, we estimated the impact of the proposed architecture on the energy density enhancement. Our architecture is compatible with various active materials; from conventional active materials to the emerging high-capacity materials. It is clear that the increased content of active materials in the cells directly lead to the increased energy density. We quantified the enhancement by selecting one set each for the former (LCO and graphite) and the latter (S and Si). Different papers report different calculation bases for energy densities. Thus we calculated the energy density via three different

bases; per mass of active materials, per mass of electrodes, and per mass of total cell. We assume the same weight fractions for electrolyte and balance of system as those of the current benchmark of Panasonic NCR18650B battery and the target structure of future Li-S battery that had been analyzed in detail by Hagen et al. [14]. Table S3.3 shows the results for full cells with the conventional active materials (LCO and graphite). Energy density per active materials is the same for the two architectures (Panasonic and Ours), but the practical energy density per total cell is enhanced by 25%–213 and 266 W h/kg based on the measured and theoretical capacity values, respectively. Table S3.4 shows the results for full cells with the emerging materials (S and Si), for which we have recently reported using S-CNT positive electrode and Li_xSi-CNT negative electrode [9]. We need CNT at ~30 wt% in these electrodes to pull out the potential of S and Li_xSi. Again, energy density per active materials is the same for the two architectures (Li-S future and Ours), but the practical performance per total cell is enhanced significantly by 54%–280 and 472 W h/kg based on the measured and theoretical capacity values, respectively, owing to the absence of the heavy Cu and Al foils. It should be noted that the very high energy density values reported in literatures often ignore the weight of the passive components such as electrolyte and balance of system.

3.4 Conclusions

In summary, the BNNT separator was developed by a simple dispersion-filtration process without using any organic components. The BNNT separator had self-supporting, flexible, and porous features with an excellent thermal stability at 500 °C. The thermal stability is much higher than that of the BNNT-coated PP separator (150 °C) reported recently [20]. The BNNT separator showed a separator performance equivalent to the conventional PP separator while decreasing the areal mass of the separator to 66% (0.7 mg cm^{-2} for BNNT vs 1.1 mg cm^{-2} for PP). The BNNT separator was combined with the CNT-based electrodes to create an electrode/separator stack without using any organic polymer nor metallic foils. The graphite-CNT/BNNT/LCO-CNT stack was thermally stable at 500 °C, and the cell made with the heated stack and fresh electrolyte worked correctly without any

degradation. The nanotube-based architecture enabled reduced mass fraction of non-active materials (6.4%) in the electrode/separator stack. This architecture, without using any organic component, makes the batteries lighter and safer, and will enable batteries that are operable at high temperature by using ionic liquid or solid electrolytes.

Acknowledgements

The authors thank BNNT, LCC for the BNNT powder sample. This work is financially supported by Grand-in-Aid for Scientific Research (S) from the Japan Society for the Promotion of Science (grant number JP16H06368). We thank Dr. Mochen Li for the nitrogen volumetric adsorption measurement. The TG-DTA analysis was conducted at Materials Characterization Central Laboratory, Waseda University.

Supplementary

Table S3.1. Weight distribution of the materials in the electrode/separator stack calculated for the current benchmark of Panasonic NCR18650B battery based on the report by Hagen et al. [14].

		Mass g	Area cm^2	Areal mass mg cm^{-2}	Mass fraction
Positive electrode	Active material [a)]			50.20	48.9%
	Additive [b)]			5.58	5.4%
	Current collector [c)]			4.05	3.9%
	Subtotal	20	334.3	59.83	
Separator	PP [c)]	1.5	372.1	4.03	3.9%
Negative electrode	Active material [a)]			26.77	26.1%
	Additive [b)]			2.97	2.9%
	Current collector [d)]			8.96	8.7%
	Subtotal	14.4	372.1	38.70	
Stack	Total			102.56	100.0%

[a)] 90% of the composite layer.

[b)] 10% of the composite layer.

[c)] 15 μm-thick Al foil.

[d)] 10 μm-thick Cu foil.

[e)] Two sheets of separators for one-set of double-faced positive and negative electrodes.

Table S3.2. Weight distribution of the materials in the cell of this work (Fig. 3.4d).

		Mass mg	Area cm^2	Areal mass mg cm^{-2}	
Positive electrode	LCO	7.294	0.50	14.51	68.6%
	CNT	0.226	0.50	0.45	2.1%
	Subtotal	7.520	0.50	14.96	
Separator	BNNT	0.848	1.13	0.75	3.5%
Negative electrode	Graphite	2.684	0.51	5.27	24.9%
	CNT	0.083	0.51	0.16	0.8%
	Subtotal	2.767	0.51	5.44	
Stack				21.15	100.0%

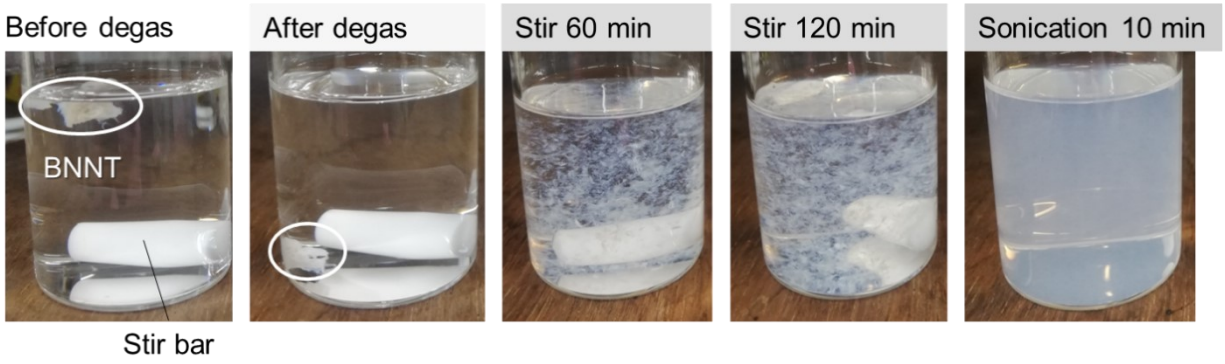

Fig. S3.1. The efficient dispersion method of BNNT. In order to fabricate a BNNT paper with a uniformly developed fine structure, it is necessary to loosen the bundles well by ultrasonic dispersion, but longer-time dispersion may make the tubes shorter and make the paper weaker. Degassing and pre-stirring were effective to complete ultrasonic dispersion in a short time. Degassing is necessary to prevent BNNT puff ball from floating in the alcohol. Pre-stirring is effective for micronizing to a certain extent with a small damage and increasing efficiency of ultrasonic dispersion. With this process of degassing and pre-stirring, ultrasonic dispersion was completed in 10 min, whereas it used to take more than 20 min.

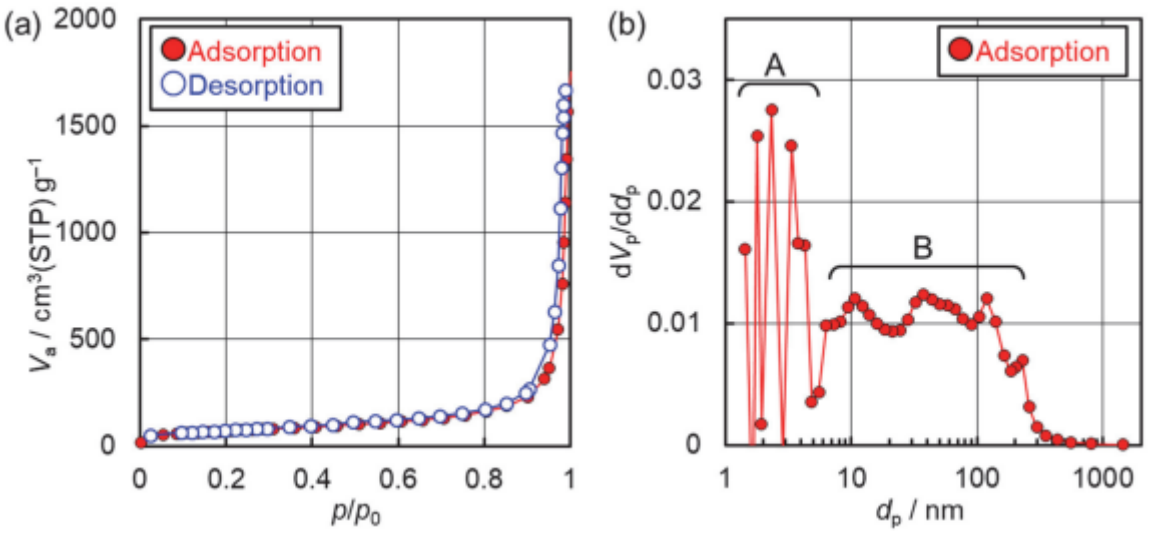

Fig. S3.2. Surface area and pore size analysis of the BNNT separator by nitrogen volumetric adsorption at –196 ºC (BELSORP-mini II, MicrotracBEL Corp., Osaka, Japan). (a) Nitrogen adsorption/ desorption isotherm with Type II characteristics typical for non-porous or macroporous materials [19]. SSA is estimated to ~250 m^2 g^{-1} (227 and 267 m^2 g^{-1} from adsorption and desorption, respectively). (b) BJH-plot of the adsorption data, showing pores of two different types, A and B, with volume fractions of A << B (note that the x-axis is in logarithmic scale). The pore A has a size of 1–5 nm, possibly corresponding to the inner part of individual BNNT and interspace between BNNTs in each bundle. The pore B has a wide size range of 6–200 nm, corresponding to the mesopores and macropores originating from the sponge-like structure made of BNNT bundles seen in the SEM images (Fig. 3.3 c,d).

Table S3.3. Cell performances estimated for the conventional architecture and the proposed architecture with conventional active materials (LCO and graphite).

Weight fraction (wt%)	Panasonic [a]	Ours [b]	Enhancement
Current collector	9.4	0.0	
Active materials	55.0	69.0	
Additives	6.1	2.1	
Separator	3.2	2.6	
Electrolyte	9.1	9.1	
Balance of system	17.2	17.2	
Total	100.0	100.0	
Fraction of active materials	55.0	69.0	
Fraction of electrodes	70.5	71.1	
Cell performance based on experimental data [c]			
LCO-measured (mA h/g) [c]	110	110	
Gr-measured (mA h/g) [c]	299	299	
Voltage (V) [c]	3.85	3.85	
N/P capacity ratio (-)	1.0	1.0	
Active materials (g/A h)	12.4	12.4	
Energy density per active materials (W h/kg)	310	310	0%
Energy density per electrode (W h/kg)	241	300	24%
Energy density per total cell (W h/kg)	170	213	25%
Cell performance based on theoretical values [d]			
LCO-theoretical (mA h/g) [d]	137	137	
Graphite-theoretical (mA h/g) [d]	372	372	
Voltage (V) [d]	3.85	3.85	
N/P capacity ratio (-)	1.0	1.0	
Active materials (g/A h)	9.99	9.99	
Energy density per active materials (W h/kg)	385	385	0%
Energy density per electrode (W h/kg)	300	374	24%
Energy density per total cell (W h/kg)	212	266	25%

a) Panasonic NCR18650B. Weight fraction data from ref. [14].

b) Assuming the same weight fractions for electrolyte and balance of system as those of Panasonic.

c) Performance is calculated based on the weight fraction of each architecture with the measured values for capacity and cell voltage in this work.

d) Performance is calculated based on the weight fraction of each architecture with the theoretical values for capacity and cell voltage.

Table S3.4. Cell performances estimated for the conventional architecture and the proposed architecture with emerging active materials (sulfur and silicon).

Weight fraction (wt%)	**Li-S future** [a]	**Ours** [b]	**Enhancement**
Current collector	12	0.0	
Active materials	17.43	26.8	
Additives	7.47	11.5	
Separator	2.8	1.4	
Electrolyte	32.6	32.6	
Balance of system	27.7	27.7	
Total	100.0	100.0	
Fraction of active materials	17.4	26.8	
Fraction of electrodes	36.9	38.3	
Cell performance (based on experimental data) [c]			
S-measured (mA h/g)	1200	1200	
$Li_{3.75}Si$-measured (mA h/g)	1350	1350	
Voltage (V)	1.72	1.72	
N/P capacity ratio (-)	1.1	1.1	
Active materials (g/A h)	1.65	1.65	
Energy density per active materials (W h/kg)	1043	1043	0%
Energy density per electrode (W h/kg)	493	730	48%
Energy density per total cell (W h/kg)	182	280	54%
Cell performance (based on theoretical values) [d]			
S-theoretical (mA h/g)	1672	1672	
$Li_{3.75}Si$-theoretical (mA h/g)	1857	1857	
Voltage (V)	2.0	2.0	
N/P capacity ratio (-)	1.0	1.0	
Active materials (g/A h)	1.14	1.14	
Energy density per active materials (W h/kg)	1760	1760	0%
Energy density per electrode (W h/kg)	831	1232	48%
Energy density per total cell (W h/kg)	307	472	54%

a) Panasonic NCR18650B. Weight fraction data from ref. [14].

b) Assuming the same weight fractions for electrolyte and balance of system as those of Li-S future.

c) Performance is calculated based on the weight fraction of each architecture with the measured values for capacity and cell voltage in ref. [9].

d) Performance is calculated based on the weight fraction of each architecture with the theoretical values for capacity and cell voltage.

References

[1] T. Placke, R. Kloepsch, S. Dühnen, M. Winter, Lithium ion, lithium metal, and alternative rechargeable battery technologies: the odyssey for high energy density, J. Solid State Electrochem. 21 (2017) 1939–1964.

[2] S. Abada, G. Marlair, A. Lecocq, M. Petit, V. Sauvant-Moynot, F. Huet, Safety focused modeling of lithium-ion batteries: a review, J. Power Sources 306 (2016) 178–192.

[3] P. Arora, Z.(J.) Zhang, Battery separators 104 (2004) 4419–4462.

[4] H. Lee, M. Yanilmaz, O. Toprakci, K. Fu, X. Zhang, A review of recent developments in membrane separators for rechargeable lithium-ion batteries, Energy Environ. Sci. 7 (2014) 3857–3886.

[5] F. Zhang, X. Ma, C. Cao, J. Li, Y. Zhu, Poly(vinylidene fluoride)/SiO2 composite membranes prepared by electrospinning and their excellent properties for nonwoven separators for lithium-ion batteries, J. Power Sources 251 (2014) 423–431.

[6] Y. Li, H. Pu, Y. Wei, Polypropylene/polyethylene multilayer separators with enhanced thermal stability for lithium-ion battery via multilayer coextrusion, Electrochim. Acta 264 (2018) 140–149.

[7] J. Li, Q. Zhong, Y. Yao, S. Bi, T. Zhou, X.M. Guo, et al., Electrochemical performance and thermal stability of the electrospun PTFE nanofiber separator for lithium-ion batteries, J. Appl. Polym. Sci. 135 (2018) 46508.

[8] K. Hasegawa, S. Noda, Lithium ion batteries made of electrodes with 99 wt% active materials and 1 wt% carbon nanotubes without binder or metal foils, J. Power Sources 321 (2016) 155–162.

[9] K. Hori, Y. Yamada, T. Momma, S. Noda, High-energy density LixSi-S full cell based on 3D current collector of few-wall carbon nanotube sponge, Carbon 161 (2020) 612–621.

[10] Y. Meng, H. Wu, Y. Zhang, Z. Wei, A flexible electrode based on a three dimensional graphene network-supported polyimide for lithium-ion batteries, J. Mater. Chem. A 2 (2014) 10842–10846.

[11] H.-C. Tao, L.-Z. Fan, Y. Mei, X. Qu, Self-supporting Si/Reduced Graphene Oxide nanocomposite films as anode for lithium ion batteries, Electrochem. Commun. 13 (2011) 1332–1335.

[12] Y. Cui, S.I. Kundalwal, S. Kumar, Gas barrier performance of graphene/polymer nanocomposites, Carbon 98 (2016) 313–333.

[13] Y. Chen, J. Zou, S.J. Campbell, G.L. Caer, Boron nitride nanotubes: pronounced resistance to oxidation, Appl. Phys. Lett. 84 (2004) 2430–2432.

[14] M. Hagen, D. Hanselmann, K. Ahlbrecht, R. Maça, D. Gerber, J. Tübke, Lithium–sulfur cells: the gap between the state-of-the-art and the requirements for high energy battery cells, Adv. Energy Mater. 5 (2015) 1401986.

[15] Z. Chen, D.Y. Kim, K. Hasegawa, T. Osawa, S. Noda, Over 99.6 wt%-pure, submillimeter-long carbon nanotubes realized by fluidized-bed with careful control of the catalyst and carbon feeds, Carbon 80 (2014) 339–350.

[16] C. Zhi, Y. Bando, C. Tang, D Golberg, Specific heat capacity and density of multi-walled boron nitride nanotubes by chemical vapor deposition, Solid State Commun. 151 (2011) 183–186.

[17] H. E. Naguib, C. B. Park, Strategies for achieving ultra low-density polypropylene foams, Polymer Eng. Sci. 42 (2002) 1481–1492.

[18] D.E. Glass, J.-P. Jones, A.V. Shevade, D. Bhakta, E. Raub, R. Sim, et al., High temperature primary battery for Venus surface missions, J. Power Sources 449 (2020) 227492.

[19] M. Thommes, K. Kaneko, A.V. Neimark, J.P. Olivier, F. Rodriguez-Reinoso, J. Rouquerol, et al., Physisorption of gases, with special reference to the evaluation of surface area and pore size distribution (IUPAC Technical Report), Pure Appl. Chem. 87 (2015) 1052–1069.

[20] M.M. Rahman, S. Mateti, Q. Cai, I. Sultana, Y. Fan, X. Wang, C. Hou, Y. Chen, High temperature and high rate lithium-ion batteries with boron nitride nanotubes coated polypropylene separators, Energy Storage Mater. 19 (2019) 352–359.

Chapter 4. Development of rechargeable Li and Li-ion batteries that work at high temperatures

4.1 Objective

Toward their further utilizations and versatile applications, an improvement of energy density and thermal stability is demanded. The operation temperatures of lithium-ion battery and sodium-sulfur battery, which are well-known and commercialized, are room temperature and above 250 °C, respectively. However, a battery working at middle temperature (60–250 °C) is not common [1]. It is demanded for exploration of space or status check of hot device such as an engine of a vehicle. In terms of battery performance, the increase of operating temperature may give both positive and negative effects [1–3]. The advantage is that ion transport and charge transfer reaction will be promoted. However, side reaction and decomposition of the components will also occur easily, and they shorten the lifetime. These disadvantages have been disturbing the realization of that kind of battery. Therefore, thermally and electrochemically stable materials should be developed and combined appropriately.

At high temperature, decrease of adhesive force of polymer binder in the electrodes will cause a problem of active material detachment. Also, the polyolefin separators are not suitable for high temperature operation due to pore closure and short-circuit problems caused by thermal shrinkage. In the previous chapter, the high thermal stability of nanotube-based architecture over 500 °C was confirmed. Therefore, the issues of polymer binder and separator may be solved by using CNT and BNNT, respectively. However, the issue of electrolyte still remained. Here, the battery working at high temperature ≥ 100 °C was considered by using the nanotube-based architecture and thermally stable electrolyte.

Ionic liquid (IL) was selected for a solvent of thermally stable electrolyte. As the cation, organic and nitrogen-containing species are the most considered due to the easiness of raw procurement, variety, safety, and cost. Two ILs with different structures were selected, one is *N*-Methyl-*N*-propylpiperidinium bis(trifluoromethanesulfonyl)imide (PP13-TFSI, alicyclic structure), the other is

1-ethyl-3-methylimidazolium bis(trifluoromethylsulfonyl)imide (EMIM-TFSI, aromatic structure). Fig. 4.1 shows the molecule structure of ionic liquids. It is known that quaternary ammonium cations are suitable compared to tertiary ammonium cations because of the resistivity to reduction. The melting point, viscosity, ionic conductivity differs depending on the length of carbon chain and the structure of cyclic or chain. These physical properties should be considered well, and PP13-TFSI has relatively low melting point of 8.3 °C and wide potential window, but the viscosity is high among the similar structure ILs [4].

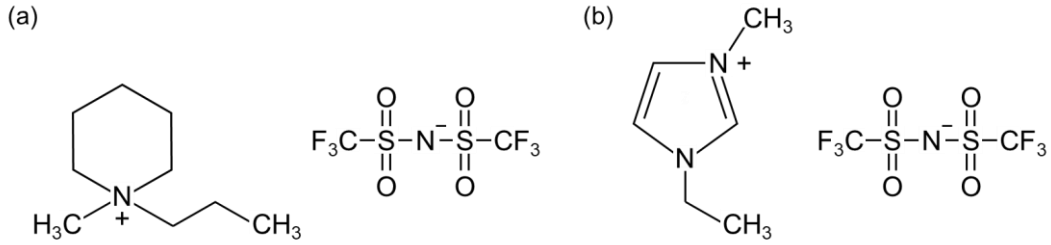

Fig. 4.1. Molecule structure of ionic liquids. (a) PP13-TFSI. (b) EMIM-TFSI.

Table 4.1. Physical properties of ionic liquid electrolyte [4].

IL	m.p. (°C)	Viscosity at 25 °C (mPa S)	Conductivity at 25 °C (mS cm^{-1})
PP13-TFSI	8.7	117	1.51
EMIM-TFSI	−15	34	10.8

4.2 Experimental

4.2.1 Fabrication of CNT-based electrodes and BNNT separator

$Li_4Ti_5O_{12}$ (LTO, TOSHIMA Manufacturing, Japan) and $LiFePO_4$ (LFP, 3.6 mass% carbon coated, TOSHIMA Manufacturing, Japan) were chosen as thermally stable active materials. CNTs synthesized through fluidized bed method [5–7] were used, which had length of ~100 μm, average diameter of 14 nm, a specific surface area of 187 $m^2\ g^{-1}$. The CNT with a small SSA was selected to suppress the side reaction, that was discussed in Chapter 2. LTO-CNT and LFP-CNT composite

papers were prepared via ultrasonication-filtration method. The powder of active material and CNT were weighed for 97:3 mass ratio, and co-dispersed in 2-propanol (IPA, FUJIFILM Wako Pure Chemical Industries, Japan) through ultrasonication (bath-type VS-50R, VELVO-CLEAR, Japan) for 10 min. The dispersed solution was vacuum-filtrated on a membrane filter (polytetrafluoroethylene filter, Merck Millipore, USA). After that, the self-supporting paper was vacuum dried under 120 °C for >2 hours for removing IPA completely. The diameter of the electrodes was 8 mm, and the areal capacity was 0.7–0.8 mA h cm^{-2}.

The BNNT separator was prepared similarly. A BNNT puff ball (BNNT, LLC, USA; length of < 200 μm, average wall number of 2–3, specific surface area of ~400 m^2 g^{-1}) was degassed and stirred in IPA for 1 hour for breaking the BNNT agglomerate into small pieces. After that, the dispersion was dispersed via ultrasonication for 10 min, vacuum-filtrated and dried as well as the electrodes. The diameter and thickness of the separator was 12–13 mm and ~20 μm, respectively.

4.2.2 Preparation of electrolyte

Ionic liquid-based electrolytes were prepared as follows. Lithium bis(trifluoromethanesulfonyl)imide (LiTFSI, Kishida Chemical Co., Japan) was dissolved in ionic liquid of PP13-TFSI (Kanto Chemical Co., Japan). The 1M LiTFSI in PP13-TFSI was used as ionic liquid (IL) electrolyte. For comparison, another ionic liquid of EMIM-TFSI (Sigma-Aldrich, USA) was chosen and 1M LiTFSI in EMIM-TFSI was prepared similarly.

4.2.3 Electrochemical measurements

2032 type coin cells (Hohsen Corp., Japan) were assembled in a glove box (Unico, Japan) under an Ar atmosphere with H_2O and O_2 contents below 1 ppmv. In the full cell, LTO-CNT|BNNT|LFP-CNT stack was fabricated. For the half cell, 8 or 10-mmφ Li foil (500, 50, 30 μm-thick, Honjo Chemical, Japan) was used instead of LTO-CNT or LFP-CNT as counter electrode. 20 μL of 1 M LiTFSI in PP13-TFSI or 1 M LiTFSI in EMIM-TFSI was added to the stack of nanotube papers. The

galvanostatic charge-discharge was conducted using a charge/discharge system (Hokuto Denko Corp., Japan). The temperature was controlled between 25 °C and 150 °C by a thermostat (ESPEC Corp., Japan). The C-rate was set between 0.5C and 5C (1C = 150 mA g^{-1}_{LFP}). From now on, CNT and BNNT will be omitted in the description of cell composition and only active materials will be described. For example, LTO-CNT|BNNT|LFP-CNT is abbreviated and written as LTO||LFP.

4.3 Results and discussion

The self-supporting nanotube papers were fabricated by the simple ultrasonication-filtration method. The LTO-CNT, LFP-CNT electrodes and BNNT separator were flexible as shown in Fig. 4.2.

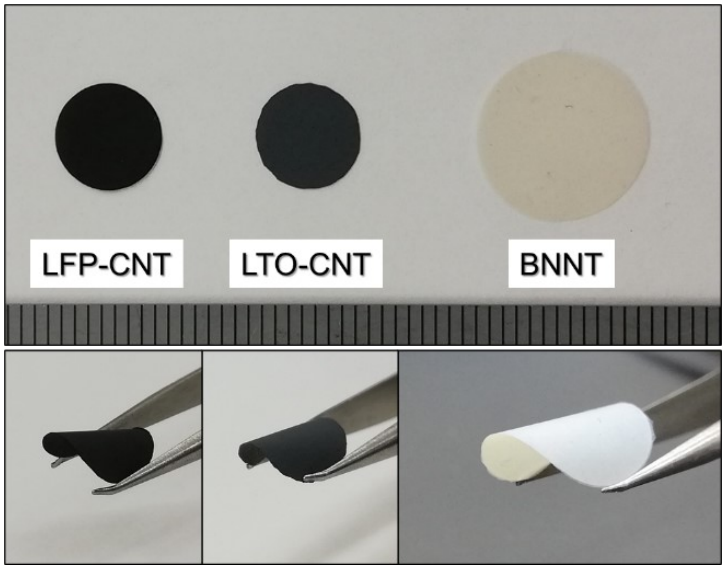

Fig. 4.2. Photos of the flexible nanotube-based papers. Left: LFP-CNT electrode. Middle: LTO-CNT electrode. Right: BNNT separator.

First, the selection of the electrolyte was studied. Charge and discharge measurements were performed on 1 M LiTFSI in EMIM-TFSI and 1 M LiTFSI in PP13-TFSI in LFP||Li (50 μm) cells. The results at 100 °C are shown in Fig. 4.3. 1 M LiTFSI in EMIM-TFSI had high initial capacity, but low Coulomb efficiency (<0.9) and rapid degradation was confirmed. In addition, the Coulombic efficiency dropped suddenly after about 200 cycles, and the cell eventually got inoperable. On the

other hand, 1 M LiTFSI in PP13-TFSI electrolyte showed long-term stable operation of more than 200 cycles. At room temperature, PP13-TFSI is known to have a wider potential window than EMIM-TFSI [4]. The stable cycle performance of PP13-TFSI would be derived from its relatively high redox resistivity even at high temperatures. Based on these results, 1 M LiTFSI in PP13-TFSI was used in this study.

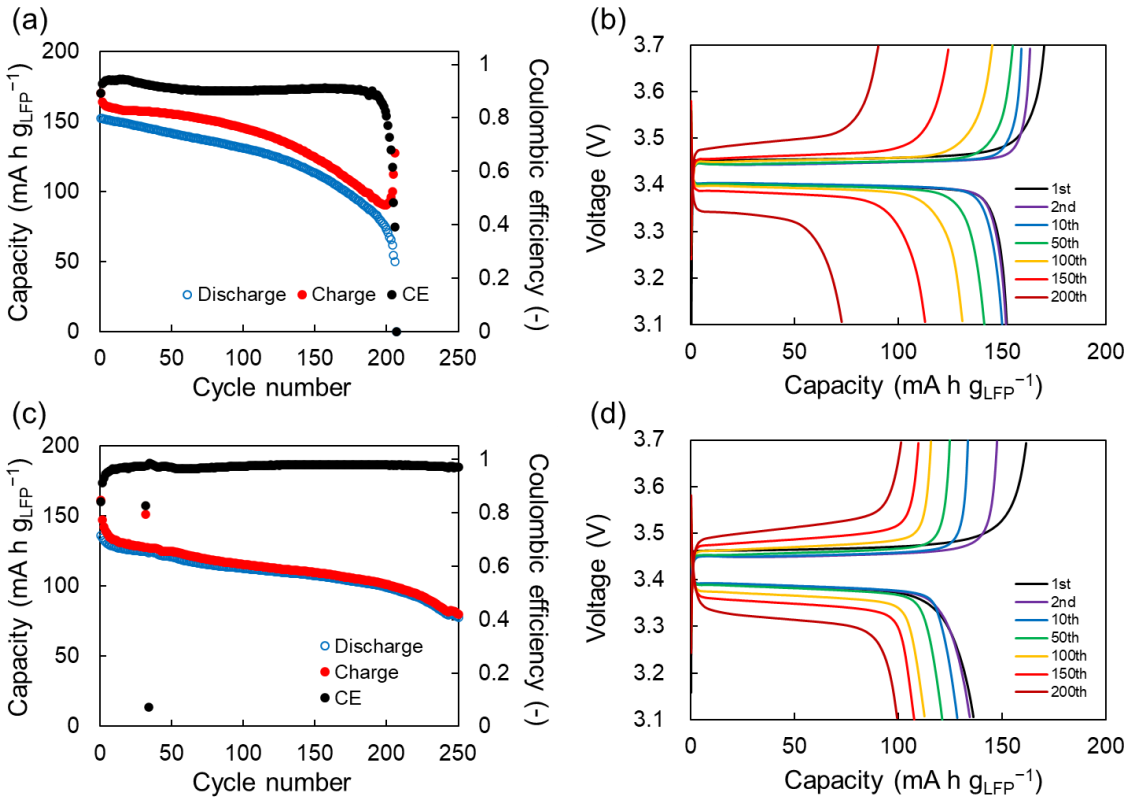

Fig. 4.3. Cycle performance and charge/discharge curves of LFP||Li (50 µm) with (a,b) 1 M LiTFSI in PP13-TFSI and (c,d) 1 M LiTFSI in EMIM-TFSI. (100 °C, 1C, SSA of CNT 187 m^2 g^{-1})

First, operability investigations about active materials of LTO and LFP were conducted in a half cell with a thick Li foil (500 µm, ~100 mA h cm^{-2}) as the counter electrode. At low temperature, the ionic conductivity was insufficient due to high viscosity, and high capacity was obtained only at low C rates of ~0.1C. When the cells were heated to 60 °C and above, they showed high capacity at 0.5C or higher because of the improved ionic conductivity. The charge-discharge results of LTO||Li (500

μm) and LFP||Li (500 μm) at 100 °C are shown in Fig. 4.4. LTO||Li (500 μm) exhibited high Coulombic efficiency of ~0.996 and long-term stable cycle performance more than 400 cycles. 1 M LiTFSI in PP13-TFSI electrolyte, LTO-CNT electrode, and Li counter electrode are found to be stable at 100 °C and in the voltage range of 0–1.9 V vs. Li. On the other hand, LFP||Li (500 μm) had a slightly lower Coulombic efficiency and the capacity gradually decreased with cycles.

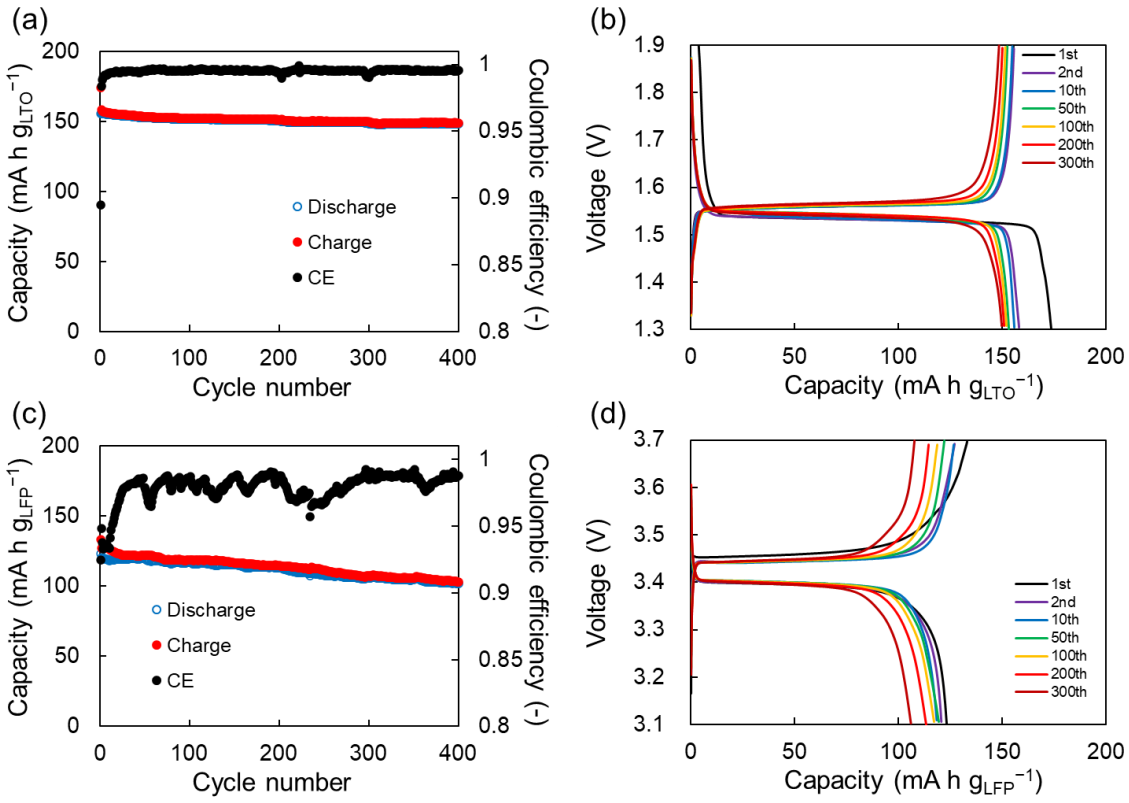

Fig. 4.4. Cycle performance and lithiation/delithiation curves of (a,b) LTO||Li (500 μm). (c,d) LFP||Li (500 μm). (100 °C, 1C, SSA of CNT 187 m^2 g^{-1})

The degradation of LFP||Li cell was studied in detail. As shown in Fig. 4.4 (c), Li 500 μm operated for more than 400 cycles with only moderate degradation. However, as shown in Fig. 4.5 (a), when the thickness of Li is reduced to 50 and 30 μm, the cycle performances deteriorated rapidly, and a sharp degradation of discharge capacity is observed after 220 and 100 cycles, respectively. The negative to positive capacity ratio (N/P) is ~13 for LFP||Li (50 μm) and ~8 for LFP||Li (30 μm). The

sharp discharge capacity degradation for the cell with thin Li foil counter electrode was not directly caused by irreversible reactions such as the decomposition of the LFP-CNT electrode or the electrolyte, but that would be caused by the active Li consumption associated with irreversible reactions. In particular, because the half cell with a thick Li foil (500 μm) counter electrode can run over 400 cycles, the decomposition of the LFP-CNT electrode should be slow (82% capacity retention after 400 cycles). And electrolyte is added at an excessive amount in these cells. Therefore, it is considered that the depletion of the active Li due to its consumption through oxidative decomposition of electrolyte is responsible for the short cycle stability of the LFP||Li (50, 30 μm). It has been reported that capacity fade of LFP at high temperature may be derived from Fe dissolution and a resistive layer forming on the negative electrode which is caused by the catalytic reaction with the reduced Fe metal when a low-potential negative electrode is used. As a solution, lithium bis(oxalate)borate (LiBOB), which is unlikely to generate strong acids such as HF, was used as an electrolyte salt instead of $LiPF_6$ to suppress Fe dissolution and long-term cycle performance was obtained [2]. As shown in Fig. 4.4 (d), there is almost no increase of overvoltage even after 400 cycles of the LFP||Li (500 μm cell), indicating that the resistance layer on the negative electrode would not be caused and was not the main cause of degradation. Because LiTFSI is used here, as with LiBOB, strong acids formation and Fe dissolution would be less likely to occur. On the other hand, the cycle stability of LFP||Li strongly depends on the Li thickness, and the amount of Li is considered to be the main factor.

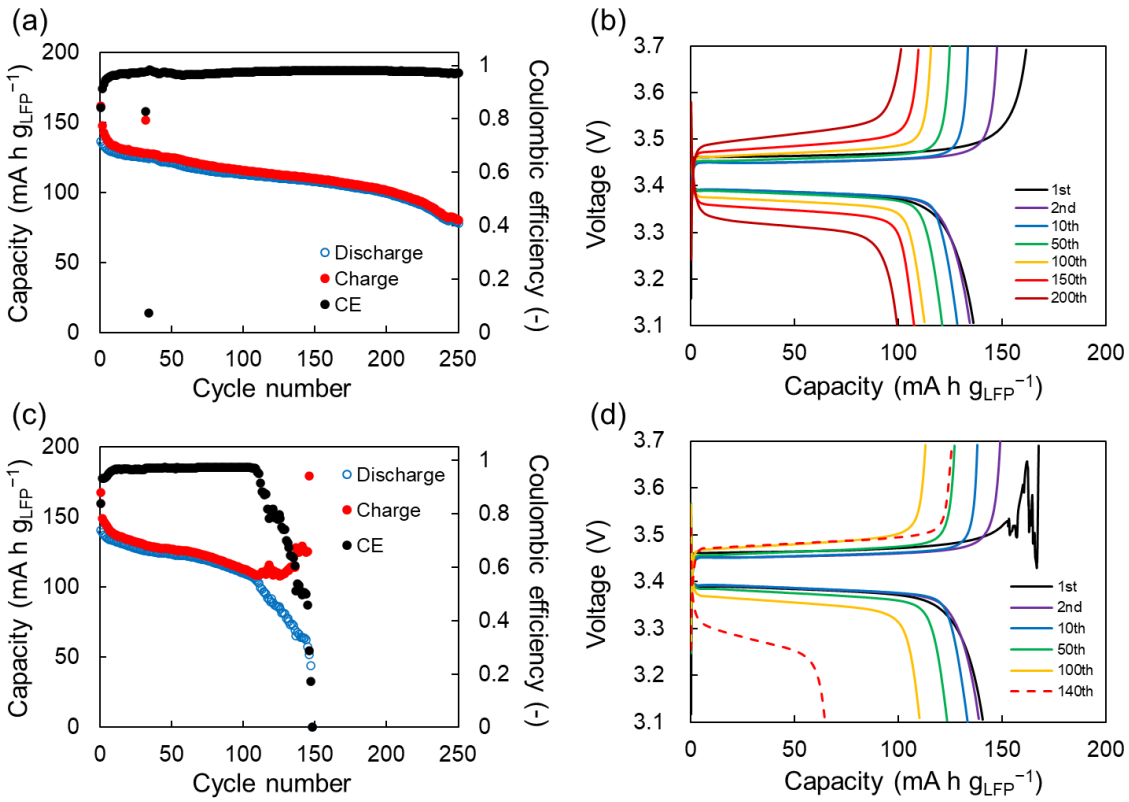

Fig. 4.5. The effect of Cycle performance and delithiation/lithiation curves of (a,b) LFP||Li (50 µm) (redisplaying of Fig.4.3 (c) and (d)). (c,d) LFP||Li (30 µm). (100 °C, 1C, SSA of CNT 187 m^2 g^{-1})

Next, the results of the C-rate dependence are shown in Fig. 4.6. From Fig. 4.5 (c) and Fig. 4.6 (a), the performance was better at 1C than at 0.5C, because of the shorter time at high potential in 1C for the same number of cycles. From Fig. 4.5 (a) and Fig. 4.6 (b) and (c), cycle stability decreased when the C-rate was further increased. This would be because oxidative decomposition of the electrolyte at the positive electrode was accelerated by overvoltage at higher C-rates as shown in Fig. 4.6 (d). Thus, it was found that the conditions for stable operation of LFP-CNT are limited by the oxidative decomposition of 1 M LiTFSI in PP13-TFSI electrolyte at high temperature.

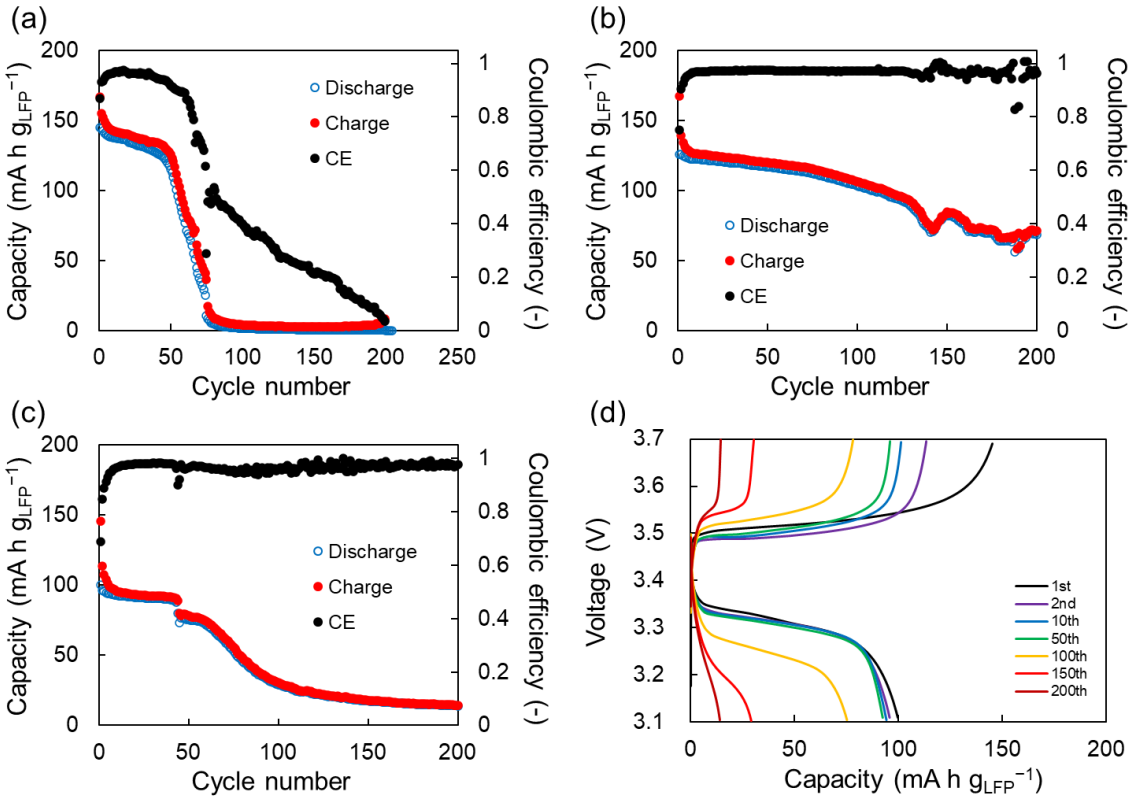

Fig. 4.6. Comparison of C-rate on LFP||Li. Cycle performance of (a) LFP||Li (30 μm) at 0.5C. (b) LFP||Li (50 μm) at 2C. (c) LFP||Li 50 μm at 5C. (d) Delithiation/lithiation curves of LFP||Li (50 μm) at 5C. (100 °C, SSA of CNT 187 m^2 g^{-1})

Here, charge/discharge measurement was conducted on LFP||LTO at 100 °C with electrodes fabricated using acetylene black and PVdF without CNT to investigate the influence of the large specific surface area of CNT. The results showed similar degradation behavior, so CNT was not the main factor of the degradation.

Based on these results, a full cell was designed. The combinations of three active material include LFP positive electrode or LTO positive electrode with a 30 or 50 μm thick of thin Li negative electrode, and LFP||LTO. At 100 °C, there was a problem of active Li depletion for LFP||LTO, and long-term cycle performance was not obtained (~90 cycles) when N/P=1 (Fig. 4.7 (a)). When N/P=1/3 (areal capacity of LFP was increased by 3 times, describe as 3LFP), the number of stable cycles increased to 150 cycles (Fig. 4.7 (c)), but the energy density per total mass of positive and

negative electrodes decreases.

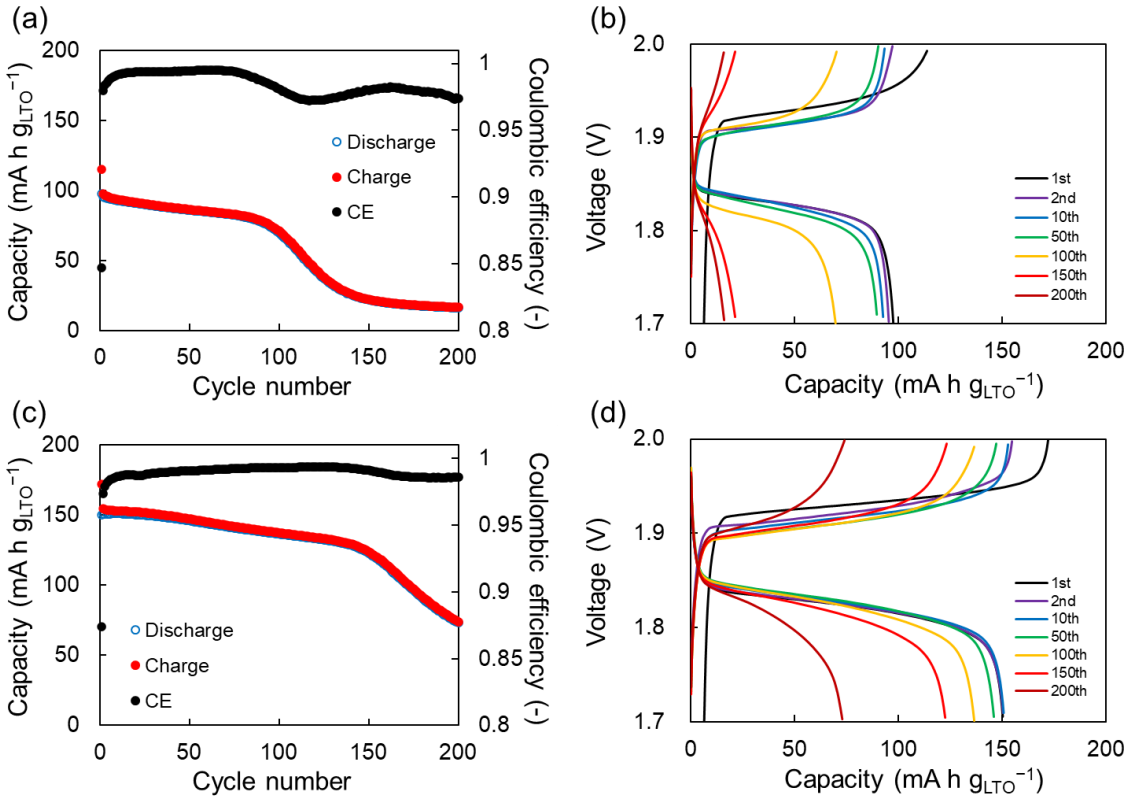

Fig. 4.7. Cycle performance and charge/discharge curves of (a,b) LFP||LTO. (c,d) 3LFP||LTO. (100 °C, 1C, SSA of CNT 187 m^2 g^{-1})

The results for LFP||Li are described above (Fig. 4.5 (a) and (b)). Although the cell voltage is as large as 3.4 V and the energy density is high, there are still issues of Li depletion and C-rate limitation.

As for LTO||Li, it was confirmed that the system operates with high Coulombic efficiency using Li 30 µm (Fig. 4.8 (a) and (b)). The Coulomb efficiency exceeded 0.998 after ~30 cycles of operation. In this cell, a short circuit was observed at the 154th cycle, which may have originated from Li dendrites. However, because Coulomb efficiency was high and the capacity degradation was small even with a thin Li 30 µm, stable operation for longer cycles is considered possible if no short circuit occurs. The combination of LTO||Li (50 µm) was also investigated at 150 °C and it worked

stably for about 200 cycles with high Coulomb efficiency of 0.997 (Fig. 4.8 (c)). At high temperatures close to the melting point of Li, the relaxation of surface roughness of Li foil, that is formed during Li deposition, should be promoted, and short circuit due to Li dendrites is expected to be less likely to occur. A novel combination of a full cell with an LTO positive electrode and a Li negative electrode, which has high Coulomb efficiency even at high temperatures, is promising as a full cell that works at high temperature.

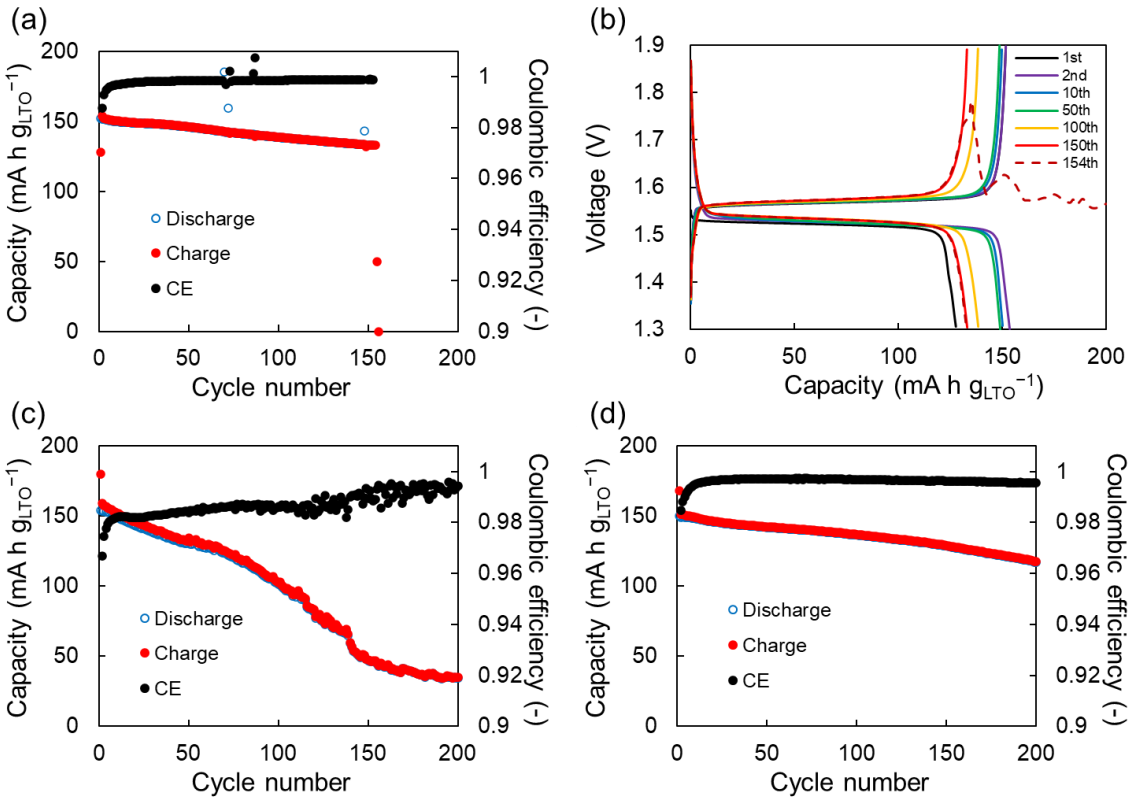

Fig. 4.8. (a,b) Cycle performance and delithiation/lithiation curves of LTO||Li (30 μm) at 1C at 100 °C. (c,d) Cycle performance of LTO||Li (50 μm) at 150 °C, (c) 1C. (d) 5C. (SSA of CNT 187 m^2 g^{-1})

4.4 Conclusion

In summary, different from room temperature operation, the activation barrier for oxidative/reductive decomposition of electrolyte is exceeded more easily in high temperature

operation, resulting in a narrower potential window for stable charge-discharge operation. Decomposition of the electrolyte and depletion of active Li are likely to become problems, and with the electrolyte selected is this research, particular attention should be paid to the oxidation side (potential of positive electrode). On the other hand, the Li negative electrode, which has been difficult to be practically use, is less likely to cause dendrite problems at higher temperature, probably because the structural relaxation of dendrites occurs when the negative electrode is operated at high temperature close to its melting point. Full cells combining Li with active materials whose potential is not too high are promising for high-temperature operating batteries.

References

[1] T. Kurita, J. Lu, M. Yaegashi, Y. Yamada, S. Nishimura, T. Tanaka, T. Uzumaki, A. Yamada, Challenges toward higher temperature operation of $LiFePO_4$, J. Power Sources 214 (2012) 166–170.

[2] K. Amine, J. Liu, I. Belharouak, High-temperature storage and cycling of C-LiFePO4/graphite Li-ion cells, Electrochemistry Communications 7 (2005) 669–673.

[3] J. Shim, R. Kostecki, T. Richardson, X. Song, K.A. Striebel, Electrochemical analysis for cycle performance and capacity fading of a lithium-ion battery cycled at elevated temperature, J. Power Sources (2002) 222–230.

[4] H. Sakaebe, H. Matsumoto, N-Methyl-N-propylpiperidinium bis(trifluoromethanesulfonyl)imide (PP13–TFSI) – novel electrolyte base for Li battery, Electrochemistry Communications 5 (2003) 594–598.

[5] D. Y. Kim, H. Sugime, K. Hasegawa, T. Osawa, S. Noda, Fluidized-bed synthesis of sub-millimeter-long single walled carbon nanotube arrays, Carbon 50 (2012) 1538–1545.

[6] Z. Chen, D. Y. Kim, K. Hasegawa, T. Osawa, S. Noda, Over 99.6 wt%-pure, sub-millimeter-long carbon nanotubes realized by fluidized-bed with careful control of the catalyst and carbon feeds, Carbon 80 (2014) 339–350.

[7] M. Li, M. Risa, T. Osawa, H. Sugime, S. Noda, Facile catalyst deposition using mists for fluidized-bed production of sub-millimeter-long carbon nanotubes, Carbon 167 (2020) 256–263.

Chapter 5. Summary and perspective

In this research, battery architecture based on electrically conducting and insulating nanotubes was proposed and developed. Research was conducted to clarify the advantages of the proposed architecture, and the full cell designs and operating conditions were studied for enhanced energy density, thermal stability, and high temperature operation.

Regarding the CNT-based electrodes, appropriate properties of CNT were revealed. Large length and SSA of CNT are appropriate for making self-supporting electrodes without metal foils or polymeric binders. In addition, large SSA provide good electrical paths to the active materials. However, excess electrolyte decomposition will be caused in the negative electrode by using CNTs with large SSAs. Therefore, CNTs with smaller SSA of ~200 m^2 g^{-1} is more appropriate for high reversible capacity under the condition of low C-rates, while those with relatively small SSA of ~300 m^2 g^{-1} is proper for obtaining higher rate performance. The amount of CNT in the electrode is only a few mass%, however, the type of CNT greatly affects performance because it has large electrically conductive surface compared to the active material. Therefore, it is necessary to consider how to keep the surface area small while maintaining the mechanical stability of the self-supporting paper as well as the conduction pathways to the active material particles. In addition, a problem remains that the porosity of CNT-based electrode is too large. It is thought that prevention of higher film density will be necessary for practical use, and further studies such as polymer binder coating are expected to be effective.

Next, BNNT separator and novel battery architecture consisted of CNT and BNNT were developed. The separator made of self-supporting sponge-like BNNT film maintained the structure and electrical insulation at high temperature of 500 °C, that is much higher than the allowable temperature for organic polymers (typically ~150 °C). Furthermore, the nanotube-based electrode/separator stack of LCO-CNT|BNNT|graphite-CNT also showed the high thermal stability of 500 °C. The cell of the heated stack with fresh electrolyte worked correctly at room temperature without degradation. In this way, lightweight and thermally stable nanotube-based architecture was

realized, and this architecture will contribute to enhance energy density and safety of batteries. This structure can also be used for applications other than rechargeable batteries, and its development into various electrochemical devices such as capacitors and sensors are also promising.

At last, high temperature operation was investigated to utilize the high thermal stability of nanotube-based architecture. Using non-volatile ionic liquid-based electrolyte, half-cells and full-cells were fabricated and evaluated for charge/discharge cycles. Under the suitable condition, stable cycle performances for ~200 cycles were achieved at 100 °C with LFP-CNT|BNNT|Li (50 μm) and 150 °C with LTO-CNT|BNNT|Li (50 μm). At high temperature, decomposition of the electrolyte and depletion of active Li become serious. Especially, the oxidative decomposition became serious for the electrolyte selected in this research. On the other hand, Li negative electrode can be more practical because the structural relaxation of dendrites will be promoted and short-circuits will less likely occur at high temperature near its melting point. Full cells made of Li and active materials with relatively low working potentials are promising for high-temperature operating batteries. The study of dendrite suppression requires the elimination of coincidence by using a large number of cells, observation of the Li surface after charge/discharge cycles. The choice of CNTs is also considered to be related to high temperature performance, and the comparison of CNTs with different SSAs is an important subject. CNTs with low SSA has low surface area for suppressed side reaction. On the other hand, those with high SSA would reduce overvoltage for suppressed oxidative/reductive side reactions on positive/negative electrodes. It is important to investigate which effect is greater for the high-temperature full cell operation. Also, the analysis of CNTs, BNNTs, active materials, and electrolyte after battery operation should also be a future project. In addition, investigations about combining other types of ionic liquid, solid electrolyte, stabilizing additive to electrolyte would be needed to obtain better performance. As another axis of evaluation, storage characteristics and calendar life should also be investigated to determine whether degradation occurs during charge/discharge or simply from exposure to high temperature.

Toward the practical uses, this nanotube-based architecture is promising for special applications that take advantage of its heat resistance rather than general-purpose applications. It is difficult to use conventional facilities because of the quite different way of battery fabrication, but it is suitable for new entrants because it can be conducted with a less complicated process such as papermaking. As discussed in Chapter 4, it is considered suitable for use in high-temperature environments, such as car engines, industrial equipment, oil drilling, and aerospace. Initially, this architecture is expected to be deployed in aerospace applications, where light weight and thermal stability are important, regardless of the cost. Production scale and cost of CNTs have been improved significantly in recent years, and since only a few mass% of CNTs are used in electrodes, cost is not an issue. On the other hand, BNNT is still in the developmental stage of synthesis, and this architecture requires a certain quantity of BNNT, so the current price (several 10,000 yen/g) is very high. In order to promote this architecture in the future, it is desirable to establish an inexpensive synthesis method for BNNTs and process technology for battery production.

The batteries with the nanotube-based architecture were realized through the simple process of dispersion and filtration by utilizing self-organizing ability of nanotubes into non-woven self-supporting films. In this way, the advantages of nanotube-based architecture for battery application, solution against the associated problems, battery design for lightweight, thermal stability, and high temperature operation were discussed.

Acknowledgements

This dissertation was completed with the guidance, cooperation and support of many people. The author would like to express my deepest appreciation. At the outset, I would like to express my sincere gratitude to my supervisor, Prof. Suguru Noda, who gave me a great deal of advice in the course of my research and dissertation writing. In addition to my research, I would like to thank for the support at various activities in our laboratory and the department. I would like to express my gratitude to Prof. Izumi Hirasawa, Prof. Toshiyuki Momma, and Prof. Masashi Okubo, my referees, for helpful discussions and comments on the manuscript. Their advice on the chemical engineering and electrochemical viewpoints enabled me to compile it into a doctoral dissertation. I would also like to thank Assist. Prof. Nobuko Hanada for her constant discussions and great support. Her frequent advice allowed me to flexibly formulate experimental plans. I also thank Mr. Toshio Osawa and Ms. Naoko Sato for their support to make my research life smooth. In addition, as I mentioned at the end of each of the relevant chapters, I would like to appreciate Dr. Li Mochen in our laboratory, Zeon Corporation, BNNT Materials, and Materials Characterization Central Laboratory at Waseda University for providing valuable samples and analysis.

Publication list

Paper

1. K. Kaneko, M. Li and S. Noda*, "Appropriate properties of carbon nanotubes for the three-dimensional current collector in lithium-ion batteries," Carbon Trends 10, 100245–100252 (2023).
2. K. Kaneko, K. Hori, and S. Noda*, "Nanotubes make battery lighter and safer," Carbon 167, 596–600 (2020).

Presentation

3. ○Kentaro Kaneko and Suguru Noda, "Nanotube-based architecture with ionic liquid electrolyte for high-temperature operation of Li and Li-ion batteries," 12th A3 Symposium on Emerging Materials: Nanomaterials for Electronics, Energy, and Environment, 2P-P25, Nishiwaseda Campus, Waseda University and Online, Tokyo, Japan, Nov. 8, 2022 (poster) (Best Poster Award).
4. ○Kentaro Kaneko, Suguru Noda, "Appropriate properties of carbon nanotube for 3D current collector of lithium-ion battery" 第 62 回フラーレン・ナノチューブ・グラフェン総合シンポジウム, 名古屋大学，愛知県名古屋市，2022 年 3 月 2-4 日.
5. ○Kentaro Kaneko, Keisuke Hori, and Suguru Noda, "Carbon nanotube and boron nitride nanotube make battery lighter and safer," 第 61 回フラーレン・ナノチューブ・グラフェン総合シンポジウム，1P-30，大阪大学オンライン開催，2021 年 9 月 1 日 (若手奨励賞 & Journal of Materials Chemistry A 賞).
6. ○Kentaro Kaneko and Suguru Noda, "Appropriate properties of carbon nanotube for 3D current collector of lithium-ion battery," International Conference on the Science and Application of Nanotubes and Low-Dimensional Materials (NT21), B77, online (hosted by Rice University, USA), June 8-10, 2021.
7. ○Kentaro Kaneko, Keisuke Hori, and Suguru Noda, "Development of highly heat-resistant battery separator based on boron nitride nanotubes," 2019 MRS Fall Meeting & Exhibit, EN02.19.08, Boston, MA, USA, December 5, 2019.
8. ○Kentaro Kaneko, Keisuke Hori, and Suguru Noda, "Highly heat-resistant battery separator based on boron nitride nanotube," 7th DGIST-Waseda Workshop on Electrochemistry 2019, Waseda Univ., Tokyo, Japan, Nov. 18, 2019.

9. ○金子 健太郎，堀 圭佑，野田 優 「窒化ホウ素ナノチューブを用いた二次電池用高耐熱性セパレータの開発」 "Development of highly heat-resistant battery separator based on boron nitride nanotubes," 化学工学会 横浜大会，D104，横浜国立大学，神奈川県横浜市，2019 年 8 月 8 日(学生奨励賞).
10. ○Kentaro Kaneko, Keisuke Hori, and Suguru Noda, "Highly heat-resistant battery separator based on boron nitride nanotube," NT19: International Conference on the Science and Application of Nanotubes and Low-Dimensional Materials, (BoA p166) P088, Wurzburg, Germany, Jul. 22, 2019.
11. ○金子 健太郎，堀 圭佑，野田 優 「窒化ホウ素ナノチューブを用いた電池用高耐熱性セパレータの開発」 "Development of highly heat-resistant battery separator based on boron nitride nanotubes," 化学工学会第 84 年会，PC201，芝浦工業大学，東京都江東区，2019 年 3 月 14 日.
12. ○金子 健太郎，堀 圭佑，杉目 恒志，花田 信子，野田 優 「ナノチューブを用いた軽量・柔軟な電池電極・セパレータの開発」 "Development of light-weight, flexible battery electrode and separator based on nanotubes," 化学工学会第 83 年会，PC205，関西大学 千里山キャンパス，大阪府吹田市，2018 年 3 月 14 日.
13. ○Tomotaro Mae, Kentaro Kaneko, Mochen Li, and Suguru Noda, "Self-supporting negative electrode of silicon monoxide held by carbon nanotubes for stable and high-capacity secondary batteries," 2022 MRS Fall Meeting & Exhibit, Boston & Virtual, Nov. 27-Dec. 2, 2022 (poster).
14. ○前 智太郎，金子 健太郎，李 墨宸，野田 優 「安定・高容量二次電池に向けた一酸化ケイ素・カーボンナノチューブ自立膜負極の開発」 第 63 回電池討論会，福岡国際会議場，福岡県福岡市，2022 年 11 月 8～10 日.
15. ○中前 快斗，吉江 優一，前 智太郎，金子 健太郎，李 墨宸，野田 優 「カーボンナノチューブ膜への活物質と塩の担持による高エネルギー密度 Li-S 電池の開発」 第 63 回電池討論会，福岡国際会議場，福岡県福岡市，2022 年 11 月 8～10 日.
16. ○Hiroki Sakurai, Kentaro Kaneko, Chiharu Tokoro, and Suguru Noda, "Simple regeneration of positive electrode using spent lithium ion battery and carbon nanotube," 12th A3 Symposium on Emerging Materials: Nanomaterials for Electronics, Energy, and Environment, 2P-P26, Nishiwaseda Campus, Waseda University and Online, Tokyo, Japan, Nov. 8, 2022 (poster).
17. ○中前 快斗，前 智太郎，金子 健太郎，李 墨宸，野田 優 「多硫化リチウムと混合支持塩を用いた Li-S 電池のエネルギー密度向上と安定動作」 "Improving energy density and

cycle performance of Li-S battery using lithium polysulfide and mixed supporting salts" 化学工学会第 53 回秋季大会， 信州大学 長野(工学)キャンパス＆オンライン，長野県長野市，2022 年 9 月 15 日.

18. ○Kaito Nakamae, Yuichi Yoshie, Tomotaro Mae, Kentaro Kaneko, Mochen Li, Suguru Noda, "High energy density Li-S battery with active materials and salts held by carbon nanotube paper," The 22nd International Conference on the Science and Application of Nanotubes and Low-Dimensional Materials (NT22), hybrid (Sungkyunkwan University in Suwon, Korea), June 19-24, 2022.
19. ○ Tomotaro Mae, Kentaro Kaneko, Mochen Li, Suguru Noda, "Self-supporting negative electrode of silicon monoxide held by carbon nanotubes for stable and high-capacity secondary batteries," The 22nd International Conference on the Science and Application of Nanotubes and Low-Dimensional Materials (NT22), hybrid (Sungkyunkwan University in Suwon, Korea), June 19-24, 2022.
20. ○中前 快斗，吉江 優一，前 智太郎，金子 健太郎，李 墨宸，野田 優 「カーボンナノチューブ膜への活物質と塩の担持による高エネルギー密度 Li-S 電池の開発」 "High energy density Li-S battery with active materials and salts held by carbon nanotube paper" 化学工学会第 87 年会，PC235，神戸大学 鶴甲第 1 キャンパス＆オンライン，兵庫県神戸市，2022 年 3 月 17 日.
21. ○前 智太郎，金子 健太郎，李 墨宸，野田 優 「安定・高容量二次電池に向けた一酸化ケイ素・カーボンナノチューブ自立膜負極の開発」 "Silicon monoxide negative electrode with self-supporting paper of carbon nanotubes for stable and high capacity secondary batteries" 化学工学会第 87 年会，J121，神戸大学 鶴甲第 1 キャンパス＆オンライン，兵庫県神戸市，2022 年 3 月 16 日.
22. ○若生 朋也，吉江 優一，前 智太郎，金子 健太郎，野田 優 「LixSi-CNT 負極の部分脱リチオ化によるリチウム二次電池の長寿命化」 "Partial delithiation of LixSi-CNT negative electrode for long-life lithium secondary battery," 化学工学会第 86 年会，PA142，オンライン，2021 年 3 月 20 日.
23. ○桜井 宏樹，前 智太郎，金子 健太郎，野田 優 「ニッケル系酸化物粒子をカーボンナノチューブで保持したリチウムイオン電池正極の開発」 "Positive Electrode of Ni-Base Oxide Particles Held by Carbon Nanotubes for Lithium-ion batteries," 化学工学会第 86 年会，PA145，オンライン，2021 年 3 月 20 日.

Patent

24. 特許公開済、野田優、金子健太郎、堀圭佑、特開 2019-149259、平成 30 年 2 月 26 日出願、令和 1 年 9 月 5 日公開

Publication

25. 金子健太郎、「若手の頭脳 ナノチューブ構造体によるリチウムイオン電池の高性能化と作製プロセスの開発」“早稲田応用化学会会報 No.105”、早稲田応用化学会、p.9、(2022.4)
26. 金子健太郎、「化学工学 第 83 巻 第 7 号」“学生会員の声 材料のアプリケーションと化学工学”、化学工学会、p.42、(2019.7.5)
27. 野田優、金子健太郎、堀圭佑、「WTLO TECHNOLOGY OFFERS」“窒化ホウ素ナノチューブ耐熱セパレータと電池部材”、早稲田大学研究推進部産学官研究推進センター(承認 TLO)、p.5、(2019.1.30)